



HAL
open science

Renewed Post-eruptive Uplift Following the 2011-2012 Rhyolitic Eruption of Cordón Caulle (Southern Andes, Chile): Evidence for Transient Episodes of Magma Reservoir Recharge During 2012-2018

Francisco Delgado, Matthew Pritchard, Sergey Samsonov, Loreto Córdova

► **To cite this version:**

Francisco Delgado, Matthew Pritchard, Sergey Samsonov, Loreto Córdova. Renewed Post-eruptive Uplift Following the 2011-2012 Rhyolitic Eruption of Cordón Caulle (Southern Andes, Chile): Evidence for Transient Episodes of Magma Reservoir Recharge During 2012-2018. *Journal of Geophysical Research: Solid Earth*, 2018, 123, pp.9407-9429. 10.1029/2018JB016240 . insu-03589317

HAL Id: insu-03589317

<https://insu.hal.science/insu-03589317>

Submitted on 25 Feb 2022

HAL is a multi-disciplinary open access archive for the deposit and dissemination of scientific research documents, whether they are published or not. The documents may come from teaching and research institutions in France or abroad, or from public or private research centers.

L'archive ouverte pluridisciplinaire **HAL**, est destinée au dépôt et à la diffusion de documents scientifiques de niveau recherche, publiés ou non, émanant des établissements d'enseignement et de recherche français ou étrangers, des laboratoires publics ou privés.

Copyright

RESEARCH ARTICLE

10.1029/2018JB016240

Special Section:

 Merging Geophysical,
 Petrochronologic and
 Modeling Perspectives to
 Understand Large Silicic
 Magma Systems

Key Points:

- InSAR evidence for three transient pulses of magma injection in the same reservoir in 6 years but with different time evolution
- Viscoelastic relaxation is less likely than magma injection to explain ground deformation signal during 2012–2015
- Crystal mush rejuvenation can occur on short timescales of a few months

Supporting Information:

- Supporting Information S1

Correspondence to:

 F. Delgado,
 delgado@ipgg.fr

Citation:

 Delgado, F., Pritchard, M., Samsonov, S., & Córdova, L. (2018). Renewed post-eruptive uplift following the 2011–2012 rhyolitic eruption of Cordón Caulle (Southern Andes, Chile): Evidence for transient episodes of magma reservoir recharge during 2012–2018. *Journal of Geophysical Research: Solid Earth*, 123, 9407–9429. <https://doi.org/10.1029/2018JB016240>

Received 20 JUN 2018

Accepted 7 OCT 2018

Accepted article online 11 OCT 2018

Published online 8 NOV 2018

Renewed Post-eruptive Uplift Following the 2011–2012 Rhyolitic Eruption of Cordón Caulle (Southern Andes, Chile): Evidence for Transient Episodes of Magma Reservoir Recharge During 2012–2018

 Francisco Delgado^{1,2} , Matthew Pritchard¹ , Sergey Samsonov³ , and Loreto Córdova⁴ 

¹Department of Earth and Atmospheric Sciences, Cornell University, Ithaca, NY, USA, ²Now at Laboratoire de Tectonique et Mécanique de la Lithosphère, Institut de Physique du Globe de Paris, France, ³Canada Centre for Mapping and Earth Observation, Natural Resources Canada, Ottawa, Ontario, Canada, ⁴Observatorio Volcanológico de los Andes del Sur (OVDAS), Servicio Nacional de Geología y Minería, Temuco, Chile

Abstract The VEI 4 rhyolitic eruption of Cordón Caulle volcano in 2011–2012 was immediately followed by ~0.77 m of exponentially decaying uplift during 2012–2015. In this study, we present evidence of additional transient pulses of inflation with interferometric synthetic aperture radar (InSAR) time series during 2016–2018. We also assess whether the 2012–2015 uplift can be explained by viscoelastic relaxation or not. InSAR detected ~12 cm of uplift during 2016–2017 and ~5 cm during 2017–2018. The three inflation episodes have very similar spatial scales and can be modeled with the same inflating sill ($z \sim 6$ km), but their time evolution is significantly different. Numerical models of a pressurized reservoir surrounded by a viscoelastic shell do not have a better fit than a magma injection model to the 2012–2015 InSAR time series, indicating that magma injection is the most likely mechanism to explain this uplift signal. The spatial similarities of the three pulses suggest that they are produced by episodic magma injection. These magma injection pulses provide the heat to remobilize the crystal mush beneath the volcano on timescales of a few months, but the end of the uplift is not predicted by existing models. None of these uplift pulses were related to abnormal seismicity, and we speculate that they are mostly aseismic because they caused stresses of lower magnitude than the co-eruptive stresses. The meter scale displacement observed at Cordón Caulle between 2007 and 2018 suggests that the volcano undergoes episodic cycles of inflation like those observed in silicic calderas.

1. Introduction

Volcanic eruptions produce a significant pressure drop with respect to the deviatoric stress in the magma reservoir walls, leading to a significant pressure gradient between a deeper source and the shallow reservoir from where magma flowed during the eruption (Segall, 2016). In some situations, the pressure gradient can trigger post-eruptive magma intrusion that can produce ground deformation signals with exponentially decaying trends (e.g., Bagnardi & Amelung, 2012; Chadwick et al., 2012; Lu et al., 2003, 2010; Reverso et al., 2014). These signals are predicted by analytical models that couple a shallow pressurized source and magma flow from a deeper source (e.g., Bato et al., 2018; Dvorak & Okamura, 1987; Lengline et al., 2008; Pinel et al., 2010). The time constant of the exponential ground deformation is a function of the magma reservoir compressibility and viscosity (Le Mével et al., 2016), theoretically allowing an estimate of the recharging magma composition and the gas content of the magma reservoir. These injection pulses also have the potential to remobilize crystal mushes located beneath active volcanoes and to trigger future eruptions (Cooper, 2017).

Alternatively, exponential signals in ground deformation data can be explained by viscoelastic relaxation (Dzurisin et al., 2009; Newman et al., 2001, 2006; Segall, 2016). In this type of model, stresses in the crust are relaxed as the pressure applied in the chamber walls is transmitted by ductile flow in the medium in which the pressurized reservoir is embedded in. These viscoelastic models (e.g., Bonafede et al., 1986; Dragoni & Magnanensi, 1989; Masterlark et al., 2010) have two important differences over the linear elastic models widely used in volcano geodesy (e.g., McTigue, 1987; Okada, 1985). First, viscoelastic simulations can explain ground deformation data with source overpressures that are closer to the tensile strength of the encasing rocks (T_s) of ~1–10 MPa (Newman et al., 2006), close to those required to trigger a dike intrusion (Rubin, 1995).

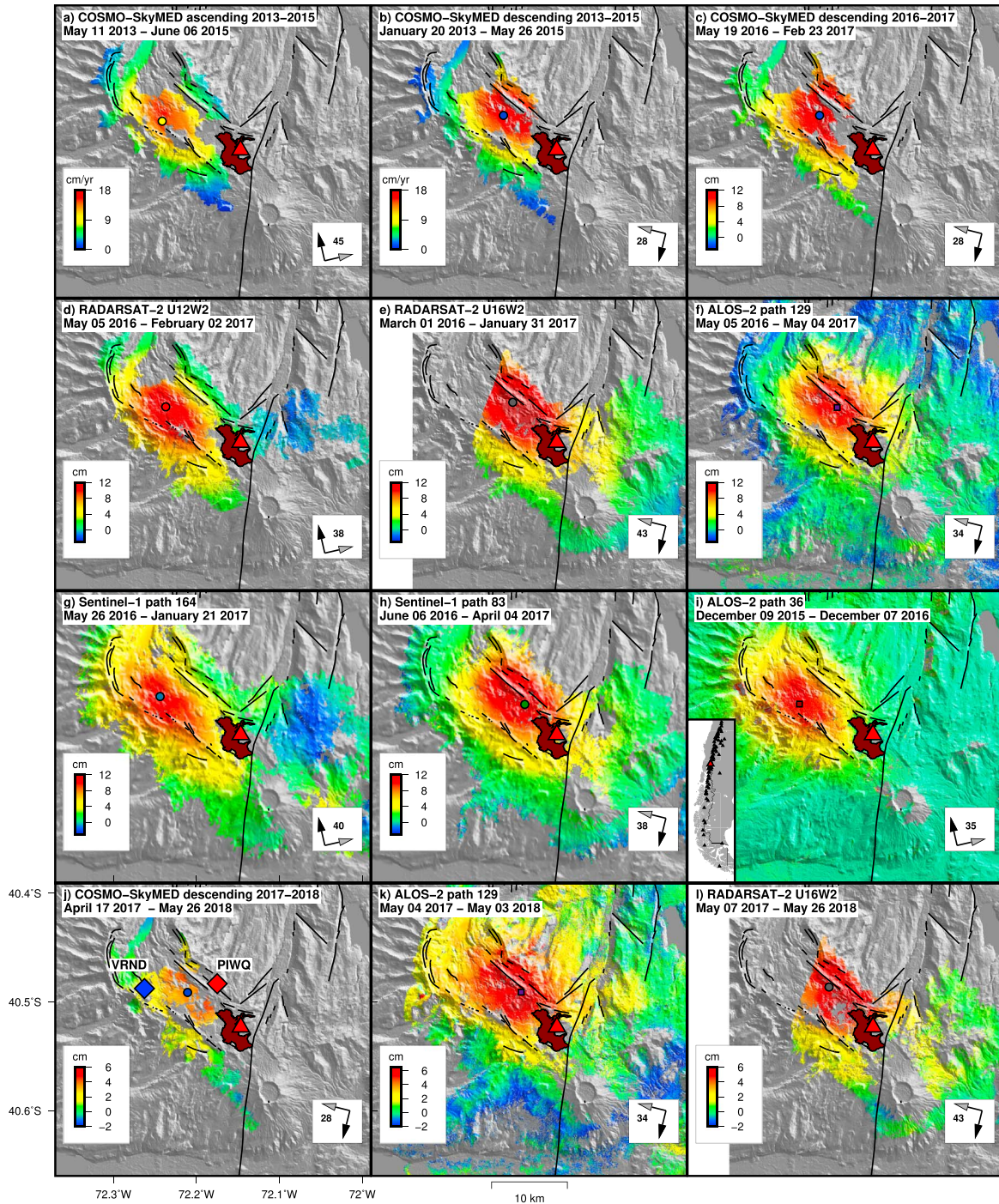


Figure 1. Mean line-of-sight surface velocities (a, b) and displacements (c–l) at Cordón Caulle from: (a) ascending CSK 2013–2015, (b) descending CSK 2013–2015 (a and b after Delgado et al., 2016, and shown for comparison with the rest of the data sets), (c) descending CSK 2016–2017, (d) ascending RADARSAT-2 2016–2017, (e) descending RADARSAT-2 2016–2017, (f) descending ALOS-2 2016–2017, (g) ascending Sentinel-1 2016–2017, (h) descending Sentinel-1 2016–2017, (i) ascending ALOS-2 2015–2016, (j) descending CSK 2017–2018, (k) descending ALOS-2 2017–2018, and (l) descending RADARSAT-2 2017–2018. The colored circles show the location of the time series maximum displacements shown in Figure 3. The thin black lines are faults, the black arrow is the satellite heading, the gray arrow is the satellite line of sight, the number in the white box is the satellite look angle, the brown outline is the lava flow erupted during 2011–2012, and the red triangle is the eruptive vent of the 2011–2012 eruption. The diamonds in (j) are the location of the continuous GPS stations. Inset in (i) shows the volcano location within South America. The red and black triangles in the inset are the Cordón Caulle 2011 eruptive and Holocene volcanoes (Siebert et al., 2010).

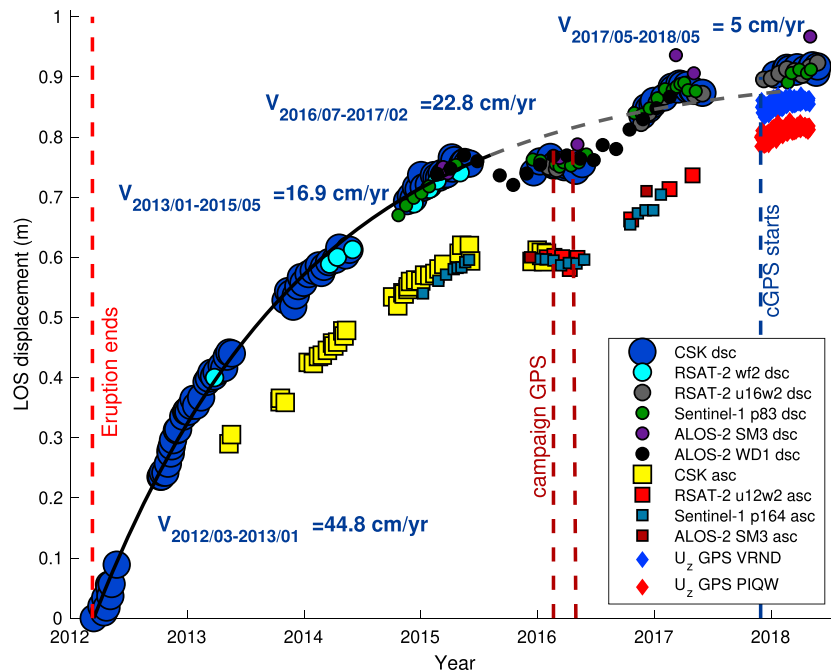


Figure 2. LOS displacements for ascending (asc, squares) and descending (dsc, circles) COSMO-SkyMED, RADARSAT-2, Sentinel-1, ALOS-2 SM3, and GPS data (shown as points of the same color in Figure 1). Abbreviations are shown in Table 1. ALOS-2 WD1 (ScanSAR) time series from Euillades et al. (2017). The black line is the best fit function of the form $U_{LOS} = U(1 - e^{-t/\tau})$ of the CSK descending data between March 2012 and May 2015 (see discussion for details). The gray dashed line shows the projection of the exponential fit to the rest of the CSK time series. The RS2, CSK, and S1 ascending time series have been offset from the CSK descending data so the end of the inflation can be better assessed in the latter. RSAT-2 WF2 and CSK ascending data are from Delgado et al. (2016) and only shown for comparison with the 2016–2017 inflation. Campaign GPS observations in February–April 2016 are described in Delgado et al. (2016) and continuous GPS (cGPS) are recorded since late November 2017 by OVDAS (Southern Andes Volcano Observatory). Velocities are only shown for the periods of ground deformation.

These are much lower and more realistic than those predicted by analytic models with overpressures that can be several orders of magnitude larger than T_s (Masterlark et al., 2010). These smaller overpressures result from the viscosity itself because the material around the reservoir transmits stresses by viscous over time, and not by a purely instantaneous elastic response. Second, viscoelastic models can produce ground deformation in the absence of chamber pressurization, implying that exponential ground deformation signals might not indicate magma recharge (Zurek et al., 2012). In the case of long-lived large silicic systems like Yellowstone and Long Valley, viscoelastic models better reflect the rheology of the materials around shallow reservoirs because the hot magma inside the reservoir is likely to have weakened the surrounding materials. Depending on the viscosity of the encasing rocks, it is possible that viscoelastic effects are important even for short-lived inflation periods following eruptions (Segall, 2016).

However, viscoelastic models are even more nonunique than the widely used linear elastic models due to the multiple choices of viscosities and rheologies as discussed here. Depending on the choice of these parameters, the signals predicted by viscoelastic relaxation models can be very similar to those produced by magma injection models (Le Mével et al., 2016). The situation can be more complicated when these exponential uplift pulses are recorded in complex sequences of transient events (e.g., Montgomery-Brown et al., 2015). As the timescales of elastic pressurization and viscoelastic relaxation can overlap, it can be challenging to differentiate among both mechanisms, leading to further ambiguities in the interpretation of geodetic signals.

In this study we focus on a sequence of three post-eruptive inflation events recorded by InSAR in 2012–2015, 2016–2017, and 2017–2018 following the 2011–2012 rhyodacitic eruption of Cordón Caulle volcano, the best instrumentally recorded silicic eruption to date (Castro et al., 2013, 2016; Jay et al., 2014). This study is divided in two parts. In the first one, we present a 6-year COSMO-SkyMED InSAR time series updated from a previous study (Delgado et al., 2016), as well as new RADARSAT-2, Sentinel-1, and ALOS-2 observations that span

Table 1
Details of the Processed SAR Data Sets

Satellite	λ (cm)	Dates (yy/mm/dd)	Pass	Path	θ	Mode, Beam	#SAR	#lfg
COSMO-SkyMED	3.1	12/03/14–18/05/26	D	N/A	28	HIMAGE, H4-02	120	404
COSMO-SkyMED	3.1	16/07/06–16/09/24	A	N/A	45	HIMAGE, H4-13	19	61
RADARSAT-2	5.5	15/05/04–17/03/30	D	N/A	35	Wide Fine 2	5	8
RADARSAT-2	5.5	16/01/30–18/05/19	A	N/A	38	U12W2	15	30
RADARSAT-2	5.5	16/02/06–18/05/26	D	N/A	43	U16W2	16	37
Sentinel-1	5.5	15/01/08–18/03/05	A	164	36	IW	25	34
Sentinel-1	5.5	14/10/23–18/05/05	D	083	38	IW	33	46
ALOS-2	24.2	15/03/12–18/05/03	D	130	34	SM3, F2-5	7	9
ALOS-2	24.2	15/12/09–17/11/22	A	36	35	SM3, F2-6	3	2

Note. The columns show the satellite name, radar wavelength (λ), date range (year/month/day), whether the satellite is in an ascending (A) or descending (D) orbit, satellite path (if available, otherwise labeled as N/A), average incidence angle (θ), mode and beam, number of synthetic aperture radar (SAR) images per track, and the number of interferograms used in the time series (lfg). For RADARSAT-2 Wide Fine 2, COSMO-SkyMED ascending, and ALOS-2 SM3 F2-6 lfg indicates the number of processed pairs. The Sentinel-1 ascending time series in Figures 1 and 2 ends in January 2017 because interferograms calculated with the next image in February 2017 have ramps that cannot be removed with simple polynomial functions. Acquisitions were then stopped in this track and resumed only during July 2017 and February–March 2018.

March 2012 to May 2018. This data set shows that after the March 2012 to May 2015 inflation, uplift resumed in July 2016 until February 2017 and since May 2017 and ongoing as of May 2018. The 2016–2017 pulse has already been documented by (Euillades et al., 2017), but here we use an independent analysis with a much larger data set. This uplift pulse was produced by the same reservoir that was active during 2012–2015, albeit at a reduced inflation rate. In the second part of this study, we address the ambiguity of interpreting posteruptive exponential ground deformation during the 2012–2015 inflation. Delgado et al. (2016) interpreted this signal as being produced by magma recharge, and here we assess whether alternative mechanisms like non-magmatic viscoelastic relaxation with exponential pressurization might explain it. Finally, we discuss the implications of these nonlinear transient reservoir recharge events in terms of crystal mush rejuvenation pulses that might lead to future eruptions in this volcano. We then compare it with other well studied silicic systems like Laguna del Maule (Le Mével et al., 2016) that have undergone recorded meter scale ground displacement over several years.

2. InSAR Data and 2016–2018 Ground Deformation

We use InSAR data from the COSMO-SkyMED (CSK), RADARSAT-2 (RS2), Sentinel-1 (S1), and ALOS-2 missions to produce time series and differential interferograms that span the complete inflation events (Figures 1, 2, and S1–S3; Table 1). These data sets were processed with standard algorithms described in detail in the supporting information (Agram et al., 2013; Chen and Zebker, 2001; Delgado et al., 2017; Farr et al., 2007; Fattahi et al., 2017; Fattahi and Amelung, 2013; Finnegan et al., 2008; Goldstein and Werner, 1998; Lopez-Quiroz et al., 2009; Prats-Iraola et al., 2012; Remy et al., 2015; Rosen et al., 2012; Samsonov, 2010; Sansosti et al., 2006; Yague-Martinez et al., 2016; Zebker et al., 2010). The differential interferograms calculated for every satellite orbit show ~ 12 cm of uplift between June 2016 and February 2017 (Figures 1c to 1i), with a mean velocity of ~ 23 cm/year (Figure 2), in agreement with an independent ALOS-2 ScanSAR time series (Euillades et al., 2017). This rate is intermediate between ~ 45 cm/year during 2012–2013 (Delgado et al., 2016) and ~ 16 – 17 cm/year during 2013–2015 (Figure 2). The onset of uplift can be inferred assuming uplift at a constant rate for the 2016 winter and then interpolating the ground displacement until it matches the period of no deformation in mid-2016. Under this assumption, the uplift likely started sometime in June–July 2017, in agreement with ALOS-2 ScanSAR data (Euillades et al., 2017). Due to the lack of coherence in the winter for all the data sets, even in 1-day CSK interferograms, it is not possible to further pin down the onset of deformation. The CSK and S1 descending and the ALOS-2 and RS2 time series do not show clear unambiguous uplift signals after February 2017; thus, we interpret this to mean that the 2016–2017 inflation event ended during February 2017. The spatial footprint of the 2016–2017 inflation is very similar to that of the 2012–2015 event (Figure 1) and different from those of the preeruptive and coeruptive deformation signals (Euillades et al., 2017; Jay et al., 2014; Wendt et al., 2017). The InSAR and GPS time series indicate an additional pulse of ~ 5 cm/year of inflation between May 2017 and May 2018 (Figure 2), although more data are required to thoroughly confirm this. As for the 2016–2017 inflation, the spatial footprint of this third posteruptive pulse is very similar to that of 2012–2015.

Table 2
Inverted Okada Source Model Parameters for the 2012–2015 (Delgado et al., 2016) and 2016–2017 Inflation Pulses

Model	X_s (km)	Y_s (km)	Z_s (km)	θ	δ	L (km)	W (km)
Sill 2012–2015	736.3	5514.2	6.2	39	11	1.9	10.07
Sill 2016–2017	736.0	5514.2	6.8	39	5	1.3	10.3

Note. X_s , Y_s , and Z_s sill centroid coordinates (UTM WGS84 18S), θ strike, δ dip, L length, and W width. The source strike θ was fixed because the signal is oriented in the NW-SE direction (Delgado et al., 2016). For a thorough description of the stability of the inversion in the absence of a proper data covariance matrix see (Delgado et al., 2016).

3. Elastic Source Modeling of Ground Deformation During 2016–2017

3.1. Elastic Modeling Approach

The differential interferograms spanning the 2016–2017 uplift (Figures 1c to 1e, 1g and 1h) were downsampled with a resolution-based algorithm (Lohman & Simons, 2005) using a horizontal sill at a depth of 4 km. This sill structure is only used to increase the number of downsampled points in the area of maximum deformation, not for the source modeling (e.g., Pearse & Lundgren, 2013). These downsampled interferograms were inverted for the best fit sill geometry (Table 2) with the nonlinear neighborhood algorithm (Sambridge, 1999). Source model error estimation (Lohman & Simons, 2005) due to atmospheric noise is not possible because the CSK differential interferogram does not have a covariance matrix due to the lack of coherence in nondeforming areas (see Delgado et al., 2016, for a detailed description of this issue). We used all the differential interferograms with equal weights for the inversion. The ALOS-2 SM3 data were not used for the source model inversion because its temporal sampling is much poorer than the rest of the data sets (Figure 2).

3.2. Elastic Modeling Results

The best fitting inverted source model for the 2016–2017 inflation is a NE-oriented subhorizontal dipping sill with a centroid at ~ 6.8 km (hereafter M_{16-17} , Table 2) and located less than 0.5 km from the centroid of the 2012–2015 inflation source (hereafter M_{12-15} , Table 2, Delgado et al., 2016). These two source models are very similar in location and dimensions because the wavelength of the 2016–2017 deformation signal is very similar to that of the 2012–2015 uplift pulse. Because the sill model still had a systematic residual, we used a variable sill opening model to calculate the volume change. We fixed the source centroid and orientation based on the uniform opening sill inversion using both M_{16-17} and M_{12-15} model and solved for opening in 10 by 20 smaller sill patches of 1×1 km² with a nonnegative least squares inversion (Delgado et al., 2016). The distributed sill opening model using M_{16-17} predicts a volume change of ~ 0.0225 km³ but with a slightly better data fit compared with a volume change of ~ 0.02 km³ for M_{12-15} , although both have similar residuals of ~ 1.5 – 2 cm (Figure 3). Because both the deformation signal and the source models of the 2012–2015 and 2016–2017 inflation events are so similar (Figure 1; Table 2), we use the M_{12-15} model to calculate the source volume change for the 2016–2017 data (Figures 3, 4, and S4).

The distributed sill model matches most of the deformation signal but with systematic residuals of ~ 1.5 – 2 cm consistent in the same areas of the ascending data sets (red boxes in Figure 3). Extending the distributed sill opening model from 10 to 15 patches in length neither improves the residual nor significantly changes the sill volume change, so the residuals could reflect a more complex deformation source (e.g., Nikkhoo et al., 2016). Similar residual signals are also observed in the same area in the 2012–2015 inflation event (e.g., Figure 3i of Delgado et al., 2016) although not as clearly as in 2016–2017 because only a single ascending track with poor coherence in the zone with largest residuals was available during the 2012–2015 uplift. The total volumetric change during 2016 and 2017 is ~ 0.02 km³, which added to the volume change of 0.125 km³ between 2012 and 2015 yields a total post-eruptive sill volume change of ~ 0.145 km³. This number is 3 times larger than the pre-eruptive source volume change of 0.05 ± 0.03 km³ between January 2007 and May 2011 (Jay et al., 2014).

4. Time-Dependent Magma Injection Models During 2012–2015

We use two different models to explain the time dependence of the 2012–2015 post-eruptive inflation signal (Figure 2). Both models assume that magma of viscosity η_m is intruded at a flow rate $Q_m(t)$ from a vertical conduit into a magma reservoir embedded in a linear elastic half space with shear modulus G and Poisson ratio ν (Figure 5). The reservoir refill increases the deviatoric stress $P_c(t)$, which leads to ground uplift. The only difference between the two models (Figure 5) is that the medium of the first one is entirely elastic (hereafter

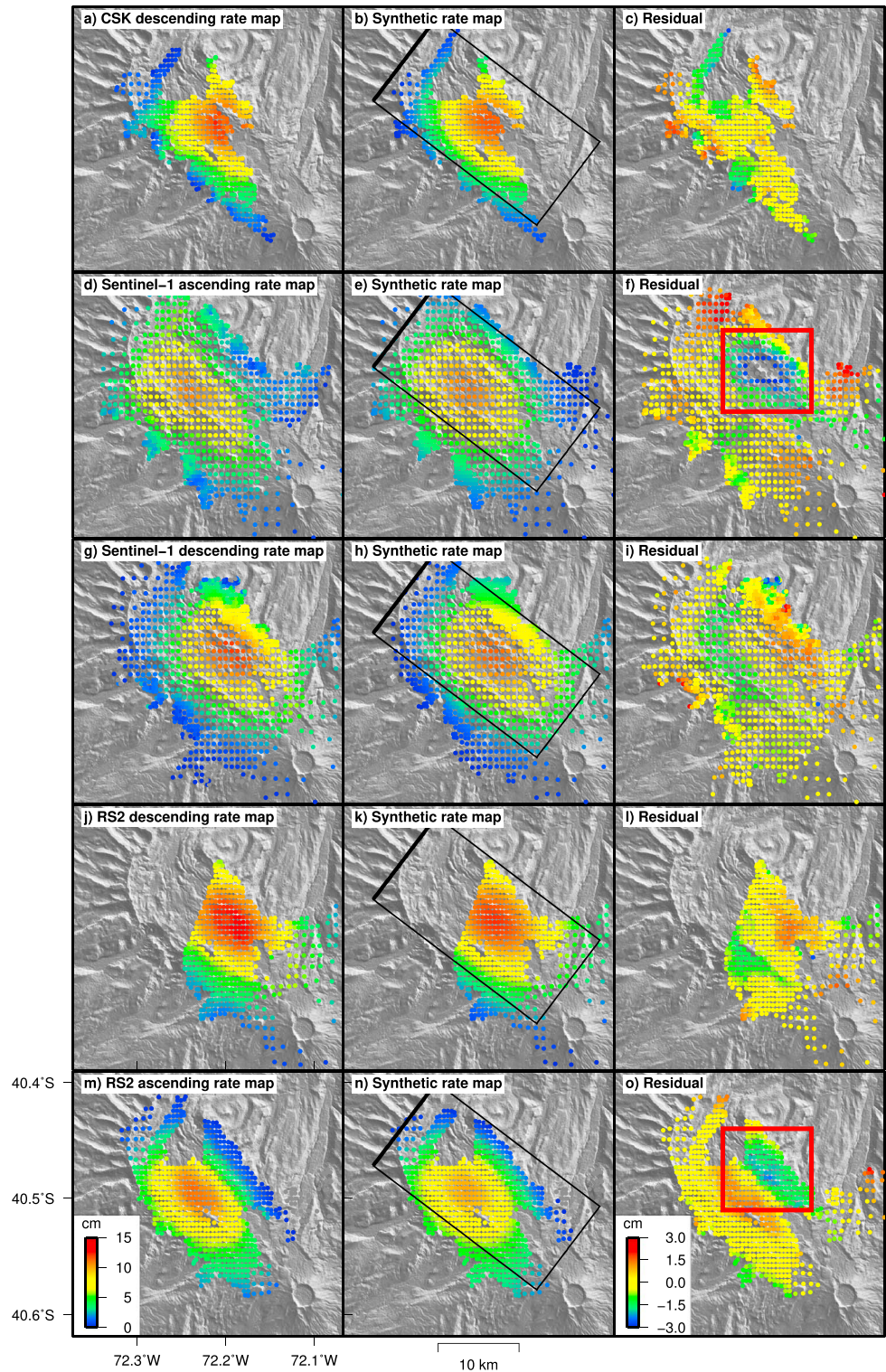


Figure 3. Downsampled InSAR deformation rate maps for the 2016–2017 inflation event (a, d, g, j, m), model prediction (b, e, h, k, n), and residuals (c, f, i, l, o) comparing data and the model for the inversion of the distributed sill opening. Black lines show the extent of the augmented sill geometry. The thin and thick black line show the outline and the top of the sill source. The color scale in (m) is the same for all the downsampled and synthetic rate maps. The color scale in (o) is the same for the all residuals. The red box in (o) and (f) shows an area with a systematic residual and is described in the text.

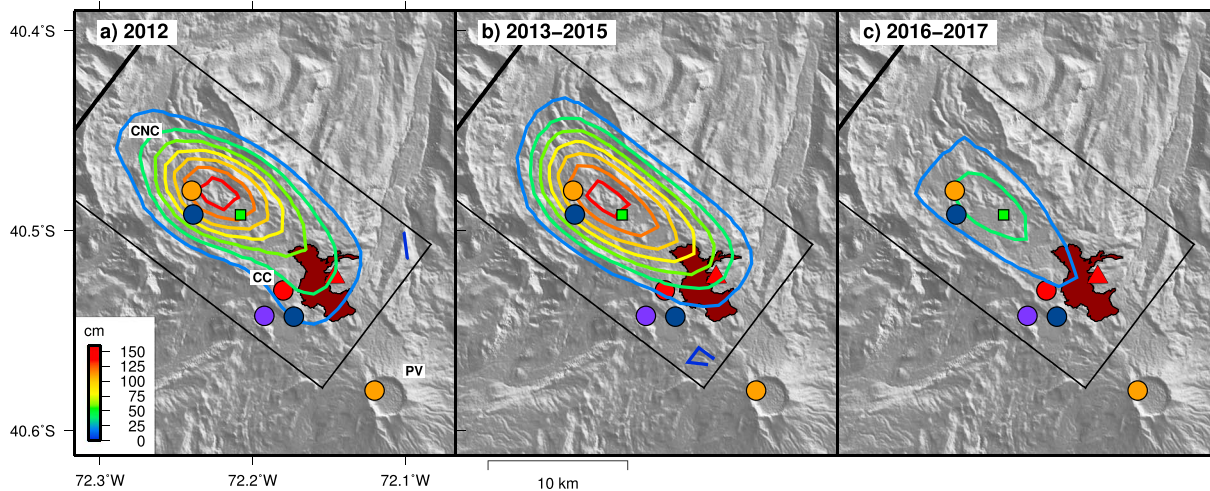


Figure 4. Contours of total sill opening for 2012–2013 (a), 2013–2015 (b), and 2016–2017 (c) draped over the shaded Shuttle Radar Topography Mission topography. Contour intervals are 25 cm of sill opening. The black rectangles show the extent of the sill models (thick line shows its top). The red triangle and brown outline are the 2011 eruptive vent and the outline of the erupted lava flow; 2012 and 2013–2015 contours after Delgado et al. (2016). Circles are inverted deformation sources (Jay et al., 2014) that deflated during the first three eruption days (orange) and between June 2011 and February 2012 (red), and inflated during 2007–2008 (blue) and 2009 (purple). The green square is the centroid of the spheroid used in the viscoelastic simulations. CNC is Cordillera Nevada caldera, CC is Cordón Caulle, and PV is Puyehue volcano.

the *analytic model*), while in the second one the reservoir is surrounded by a viscoelastic shell with viscosity η (hereafter the *viscoelastic model*) The presence of a viscous shell is plausible because it is likely that the intrusion of hot magma over several thousands of years has weakened the area around the reservoir. This implies that in addition to an instantaneous ground displacement due to pressurization in an elastic media, there is a delayed response, which is a function of the shell viscosity (Newman et al., 2001). These magma injection models require the use of a source model that incorporates the reservoir overpressure as a model parameter, so in the following sections we use the prolate spheroid model of Delgado et al. (2016) (Table 3), which also provides a very good data fit to the 2012–2015 InSAR data.

Viscoelastic effects can be tested by analyzing the data itself. The predicted ground deformation by a pressurized sphere of radius R_1 surrounded by a viscous shell of radius R_2 is equivalent to the elastic response of a sphere with radii R_1 and R_2 at the beginning and at the end of the simulation, respectively (equations 7.101 and 7.113 in Segall, 2010). This results in ground deformation signals of different wavelengths, which can be used to test for potential viscoelastic effects. Profiles of ground deformation normalized with respect to the maximum of each epoch in the time series between 2012 and 2016 show that the wavelength of the ground deformation signal does not vary significantly throughout the inflation, except during the first two

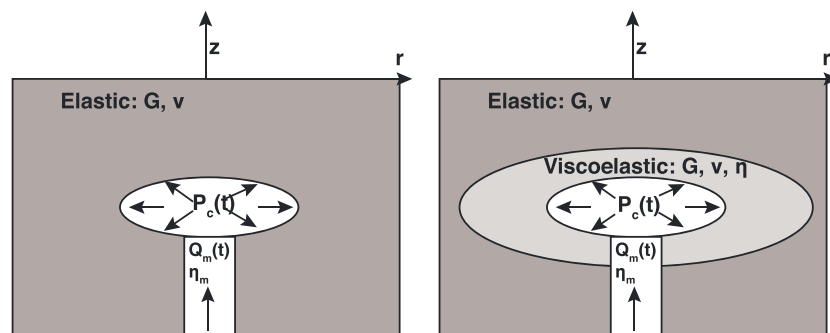


Figure 5. Cartoons that summarize the magma recharge models. In both models the reservoir is embedded in an elastic medium with shear modulus G , Poisson ratio ν , and with magma influx $Q_m(t)$ proportional to the pressure gradient. This implies that the reservoir pressure is an exponential of the form $P_c(t) = P_f(1 - e^{-t/\tau})$ (Lengline et al., 2008; Pinel et al., 2010). The only difference between the elastic (left) and viscoelastic (right) models is the shell with viscosity η in the latter.

Table 3

Inverted Prolate Spheroid (Yang et al., 1988) for the 2012–2015 Inflation Event (Delgado et al., 2016)

Model	X_s (km)	Y_s (km)	Z_s (km)	θ	δ	a (km)	b (km)
Spheroid 2012–2015	736.6	5,513.9	4.6	129	9	7.2	1.0

Note. This spheroid model can also explain the 2012–2015 data with a very low residual, and it is used in the viscoelastic simulation. Source model parameters: X_s , Y_s , and Z_s spheroid centroid coordinates (UTM WGS84 18S); θ strike; δ plunge; a semimajor axis; b semiminor axis (fixed in the inversion to ensure numerical accuracy).

and a half months of the uplift (Figure 6). This suggests that the data itself are to a first order not indicative of viscoelastic effects.

Time-dependent analysis of transient signals of volcano ground deformation has been carried out focusing on a time series from a single point that is representative of the complete ground deformation or the point of maximum uplift (e.g., Le Mével et al., 2016; Newman et al., 2006; Parks et al., 2015). To assess whether the assumption that a single time series is representative of the complete data set or not for Cordón Caulle, we fit an exponential function of the form $U = U_f(1 - e^{-t/\tau})$ to pixels that remained coherent in at least 80% of the CSK time series (Figure S5). As the time constant τ is similar for pixels near the point of maximum uplift, we consider it as representative of the complete data set. In the following sections, we apply models of magma recharge and viscoelastic relaxation to the time series of the point of maximum uplift only.

4.1. Analytic Exponential Model

The predicted ground displacement of the system made up of a pressurized spheroidal reservoir coupled to a deep source with constant overpressure has an analytic solution (Le Mével et al., 2016; Lengline et al., 2008). The ground deformation U is given by $U = U_f(1 - e^{-t/\tau})$, where U_f is a constant that is the product of the final source overpressure ΔP and terms that depend on the source geometry (Yang et al., 1988), and τ a time constant given by formula (1).

$$\tau = \frac{8\eta LV_0(\beta_m + \beta_w)}{\pi a_c^4} \quad (1)$$

Here L is the conduit length, a_c the conduit radius, η the magma viscosity, and β_m and β_w the magma and reservoir compressibilities. For the reservoir compressibility we use formula (2)

$$\beta_w = \frac{1}{G} \quad (2)$$

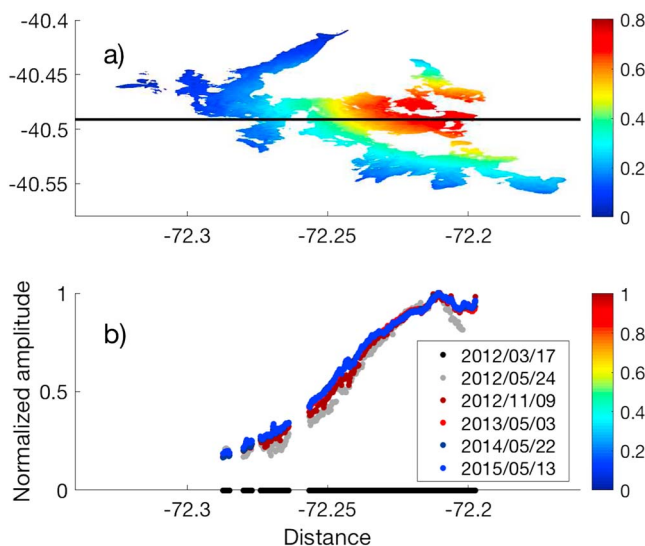


Figure 6. (a) Total line-of-sight displacement in meters at the end of the 2012–2015 inflation from the CSK descending time series. The black line is the location of the deformation profiles shown in (b). (b) Profiles of ground deformation for different times normalized with respect to the maximum of each epoch.

for a prolate spheroid (Amoruso & Crescentini, 2009), where G is the shear modulus. The key parameter to constrain is the magma viscosity η because it provides information on the composition of the magma that is flowing into the reservoir, so the time constant formula is rearranged to solve for η :

$$\eta = \frac{\tau \pi a_c^4}{8LV_0(\beta_m + \beta_w)}. \quad (3)$$

This analytic model predicts most of the ground deformation for $\tau = 1.8$ years and inverted from the CSK time series (Figure 2). However, and as noted by Delgado et al. (2016), the magma recharge model cannot explain the abrupt end of the deformation in May 2015. Given this time constant, values from the prolate spheroid model of Delgado et al., 2016 (2016; Table 3), and assuming a deep magma source in the Moho at a depth of ~ 33 km ($L = 28$ km; Hildreth & Moorbath, 1988), we estimate η as a function of both G , a_c , and β_w in Figure 7 for $\tau = 1.8$ years. We use a range of conduit radii between 1 and 50 m, slightly higher than those modeled and observed for subaerial vents (Fukushima et al., 2010), shear moduli between 10 and 32 GPa, and magma compressibilities of 0 and $2.1 \cdot 10^{-10} \text{ Pa}^{-1}$ for both incompressible and very compressible magmas (Jay et al., 2014). For a fixed conduit radius, the range of shear moduli and magma compressibilities change the magma viscosity by one order of

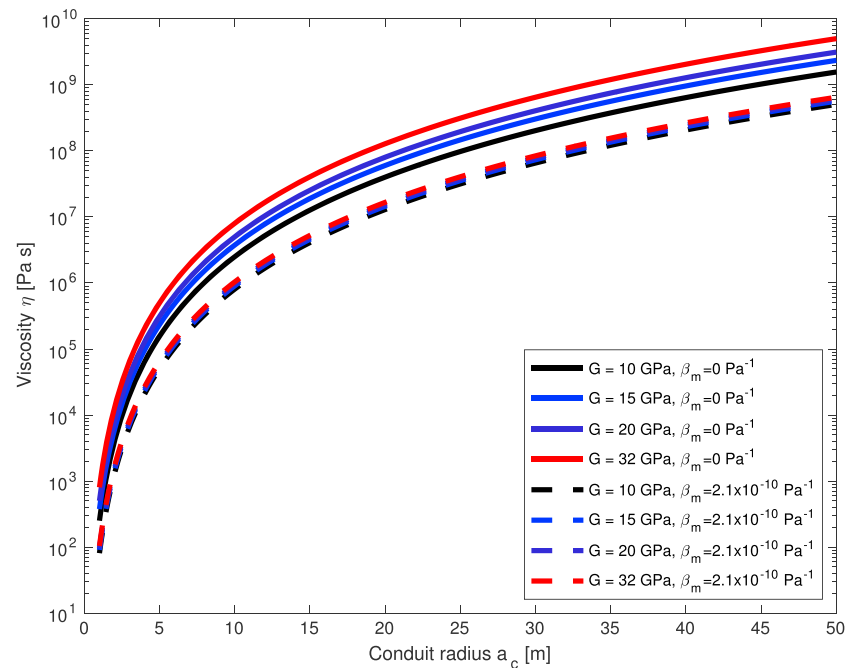


Figure 7. Magma viscosity η as a function of conduit radius a_c , magma compressibility β_m , and shear modulus G derived from the time constant τ of the best exponential fit for the CSK data set time series of Figure 2. See text for details. Solid and dashed lines show calculations for incompressible ($\beta_m = 0$) and gas-rich compressible ($\beta_m = 2.1 \times 10^{-10} \text{ Pa}^{-1}$) magmas for a set of shear moduli between 10 and 32 GPa. The calculations show that a relatively small range of conduit radii predicts a very large range of magma viscosities. The viscosity is a proxy for the magma composition, but it is not possible to assess the composition of the injecting magma in the absence of further observations to narrow the range of conduit radii.

magnitude, so the effect of G and β_w is of second order. However, the magma viscosity varies over 8 orders of magnitude for conduit radius between 1 and 50 m, almost spanning the entire range of magmas from mafic to felsic compositions, and with 0–3 wt% of dissolved H_2O (Leshner & Spera, 2015). Alternatively, the conduit radius can be calculated with knowledge of the magma viscosity, flux rate, source overpressure, and density gradients (Fukushima et al., 2010). Nevertheless, given the strong dependence of the magma viscosity on the fourth power of the conduit radius, and the lack of geophysical observations of such structures, we do not attempt to further pin down the properties of the recharging magma.

4.2. Finite Element Linear Viscoelastic Model

Analytic solutions for pressurized reservoirs surrounded by viscoelastic shells with a Maxwell rheology (Dragoni & Magnanensi, 1989; Segall, 2010, 2016) predict ground displacement with exponential decaying trends, very similar to the elastic model. But a severe limitation of viscoelastic models applied to volcano geodetic data is that these analytic solutions are available only for spherical sources with either constant, linear, trapezoidal, or exponential pressure functions (e.g., Bonafede et al., 1986; Del Negro et al., 2009; Parks et al., 2015; Segall, 2010, 2016). Hence, viscoelastic models for volcanic sources of arbitrary shapes and pressurization functions must be calculated with numerical techniques that are computationally expensive and time consuming, rendering many inversion algorithms difficult to implement.

An example of the complexity of viscoelastic simulations applied to volcano geodetic data is shown in Table 4, which highlights that there is no agreement upon the choice of viscous rheology and medium. Previous studies have relied on modeling either a single time series (e.g., Newman et al., 2001, 2006; Parks et al., 2015) and then using the synthetic model derived from the best fit parameters to predict the rest of the available data sets, or a set of total displacements (e.g., Del Negro et al., 2009; Fialko & Pearce, 2012; Gregg et al., 2013; Hickey et al., 2013; Masterlark et al., 2010; Pearce & Fialko, 2010). The reservoir pressurization functions vary from linear (Hickey et al., 2013) to highly nonlinear (Newman et al., 2001, 2006), which requires an a priori guess of the unknown pressurization time evolution. Another limitation is that the input geometry from an elastic model is potentially biased because this best fit source model may be different from that for a viscoelastic source

Table 4
Comparison of Viscoelastic Setups Used to Model Volcano Geodetic Data

Volcano	Signal	Data set	Model geometry	Viscous medium	Viscoelastic rheology	Pressure function	η (Pa·s)
Long Valley ¹	Exponential inflation	EDM TS	Spheroid 2-Dax	Shell	Maxwell	Arbitrary	Rheology and exp fits (10 ¹⁶)
Etna ²	Mean inflation	GPS vectors	Sphere 2-Dax	HS	Maxwell	Arbitrary	Power law, T 2-D
Okmok ^{3,3}	Coeruptive deflation	Interferogram	Sphere 2-Dax	Shell	Maxwell	Constant	7.5×10 ¹⁶
Socorro ⁴	Constant inflation	InSAR mean velocity	Sill 3-D	HS except upper 12 km	Power Law	Constant	10 ¹⁹ (forward)
Santorini ^{b5,1}	Transient inflation	GPS vectors	Spheroid 2-Dax	HS	GenMaxwell	Constant	5×10 ¹⁸ (fixed)
Santorini ^{b5,2}	Transient inflation	GPS TS	Sphere 3-D	Shell	Maxwell	inverted	4.7×10 ¹⁵
Taal ⁶	Transient inflation	GPS TS	Sphere 3-D	Shell	Maxwell	Arbitrary	Several
Uturuncu ^{7,1}	Constant inflation	InSAR mean velocity	Diapir 3-D	HS except upper 10 km	Maxwell	Constant	Power law, T
Uturuncu ^{7,2}	Constant inflation	Interferogram	Spheroid 2-Dax	HS except upper 5 km	Standard linear	Linear	10 ¹⁷ (fixed)
Uturuncu ^{7,3}	Constant inflation	InSAR mean velocity	2-Dax diapir	HS	GenMaxwell ($\mu_1 = \mu_2 = 0.5$)	Stepwise	Power law, T 2-D
Laguna del Maule ⁸	Exponential inflation	InSAR TS	Spheroid 2-Dax	HS	Standard linear	Constant	10 ⁶ mafic (fixed), 10 ¹² felsic (fixed)
Soufriere Hills ⁹	Constant inflation	GPS vectors	Spheroid 2-Dax	HS	GenMaxwell ($\mu_1 = \mu_2 = 0.5$)	Stepwise	Power law, T 2-D
Aira ^{c,10}	Ramped inflation	GPS TS and vectors	Spheroid 3-D	HS	Standard linear	Stepwise	Power law, T 2-D
Cotopaxi ^{c,11}	Transient inflation	EDM vectors	Spheroid 3-D	HS	Standard linear	Step	Power law, 3-D

Note. Abbreviations are as follows: 2-Dax = two-dimensional axis-symmetric model; 3-D = three-dimensional model; EDM = electronic distance measurement; HS = half space; InSAR = interferometric synthetic aperture radar; TS = time series; GenMaxwell = generalized Maxwell viscoelastic rheology. All the examples are forward models except for the following:

^aA grid search was used to search for the best fit model viscosities and pressures. ^bThe data were inverted with an analytic formula. ^cA nonlinear inversion algorithm implemented in the COMSOL Multiphysics finite element software was used. References: ¹Newman et al. (2006), ²Del Negro et al. (2009), ³Masterlark et al. (2010), ⁴Pearse and Fialko (2010), ^{5,1}Griego et al. (2013), ^{5,2}Parks et al. (2015), ⁶Galgana et al. (2014), ^{7,1}Fialko and Pearse (2012), ^{7,2}Hickey et al. (2013), ^{7,3}Gottsmann et al. (2017), ⁸Le Mével et al. (2016), ⁹Gottsmann and Odbert (2014), ¹⁰Hickey et al. (2016), and ¹¹Hickey et al. (2016).

Table 5
Seismic Wave Velocities (Wendt et al., 2017) and Densities Used in the Finite Element Model

Depth (km)	V_p (km/s)	V_s (km/s)	Density (kg/m ³)
0.0	4.70	2.65	2,650
0.5	4.90	2.81	2,650
1.5	5.05	2.84	2,650
2.5	5.10	2.87	2,650
3.5	5.15	2.92	2,650
4.5	6.05	3.40	2,650
5.5	6.38	3.62	2,650
6.5	6.46	3.63	2,650
7.5	6.47	3.63	2,650
8.5	6.50	3.65	2,700
12	6.60	3.76	2,850
15	6.70	3.88	2,850
30	6.90	4.10	3,100
45	7.00	4.27	3,230
65	7.30	4.44	3,230

Note. The density of the first 8.5 km is from the gravity model of Sepulveda et al. (2005) and was used as the background value of the upper crust. The rest of the densities are from the gravity model of Tasarova (2007).

model with elastic layering. To our knowledge, inversion algorithms that search for the complete set of best fit model parameters for a pressurized spheroid surrounded by a viscous shell (source location, geometry, rheology, and pressurization function) do not exist. The few examples of inversions of geodetic data in volcanoes with viscoelastic models have used either elastic models as the input geometry (Masterlark et al., 2010) or a viscoelastic half space rather than a shell (Hickey et al., 2016). Hence, we rely on using the elastic source models derived from nonlinear inversions as input geometries.

Given these drawbacks of viscoelastic modeling, we take the following approach for the Cordón Caulle data. First, we explore the dependence of the shell viscosity using a model for a spherical source with an exponential pressure function (Equation 7.113 of Segall, 2010), and constrained with the time constant calculated from the timescales of exponential fits to the 2012–2015 CSK time series. However, we do not use the analytic model of Segall, (2016, equation 18) because the source geometry is different than the one that deflated during the 2011–2012 eruption (Delgado et al., 2016). Second, we use finite element simulations with a grid search algorithm to calculate the shell viscosity.

4.2.1. Finite Element Model

We use the finite element method to model the ground displacement produced by a pressurized spheroidal source calculated in our previous paper (Delgado et al., 2016) and surrounded by a viscous shell. Although the preferred source geometry responsible for the 2012–2015 inflation was a subhorizontal sill, we use the spheroid model (Delgado et al., 2016) because the source overpressure is a model parameter required by the numerical simulation, and its root mean square is only slightly larger than the one of the sills. We use the Cubit software to create a 3-D mesh with linear tetrahedral elements and the finite element open source software Pylith (Aagaard et al., 2013) for the viscoelastic simulations. The mesh size was chosen to be a trade-off in terms of computational load and accuracy to benchmark well-known analytic linear elastic (McTigue, 1987; Yang et al., 1988) and linear viscoelastic solutions (Segall, 2010; Figure S6). We find that the difference between the finite element and the approximate analytic solution of Segall (2010) is at most 3% for a small pressurized sphere (Figure S6), which is well within the uncertainties of individual epochs in the CSK time series. Although other studies have assumed that most of the medium is viscoelastic (e.g., Del Negro et al., 2009; Hickey et al., 2013), we consider this an unlikely situation for the short timescales of ground deformation (months to years) and because all the preeruptive, coeruptive, and posteruptive deformation sources (Jay et al., 2014) are shallow (depths between 4 and 6 km) and located just beneath Cordón Caulle. We incorporate the effect of 1-D

elastic layering using the seismic velocity model of Wendt et al. (2017) and the density models of Tasarova (2007) and Sepulveda et al. (2005; Table 5).

The finite element simulations presented in this study have two unknowns that must be constrained after the model geometry has been set. These model parameters are the shell viscosity and the pressurization history. Literature values for shell viscosities span 1 order of magnitude, from $4.7 \cdot 10^{15}$ Pa·s (Parks et al., 2015) to $7.5 \cdot 10^{16}$ Pa·s (Masterlark et al., 2010) with an average of 10^{16} Pa·s for a felsic shell surrounding a felsic magma chamber (Newman et al., 2001). As the CSK time series follows an exponential trend recorded just after the end of the 2011–2012 eruption, and previous studies have used pressurization functions that follow the overall trend of the geodetic time series (Hickey et al., 2016; Newman et al., 2001, 2006; Parks et al., 2015), the data are consistent with a simple exponential pressurization function. Hence, we do not try complex pressure functions with transient steps (e.g., Hickey et al., 2016; Newman et al., 2001, 2006). The modeled pressure function is $P(t) = P_f(1 - e^{-t/\tau})$ (Lengline et al., 2008), with τ a time constant that we vary between 0.1 and 0.9 years and $P_f = 1\text{--}30$ MPa. Different models with lower final overpressures can be tried by just scaling P_f because the chamber overpressure is a linear parameter in the finite element model. With this pressure history, the viscoelastic finite element model parameters that must be sought for are the viscosity and the pressurization timescale.

4.2.2. Viscoelastic Rheology

A variety of linear viscoelastic rheologies are available (Table 4), including the Maxwell, generalized Maxwell, Kelvin-Voight, and standard linear solid models (Segall, 2010). The main difference between these models is the number of springs and dashpots that represent the linear elastic and viscoelastic elements, respectively, and the way they are arranged. Geodetic studies of postseismic deformation (Freed & Burgmann, 2004) have shown that in some situations the Maxwell model is inaccurate and power law rheologies are required to properly model GPS velocities. However, Table 4 shows that most of the studies have relied on either a Maxwell or generalized Maxwell rheology to simulate viscoelastic deformation at volcanoes. Only a few studies (Hickey et al., 2013, 2015, 2016; Le Mével et al., 2016; Pearse & Fialko, 2010) have used a power law and a standard linear solid medium, most likely because they have considered ground deformation with timescales of decades rather than a few years. Our calculations comparing a generalized Maxwell rheology with equal fractional components of the shear modulus ($G_1 = \mu_1 G$, $G_2 = \mu_2 G$, $\mu_1 = \mu_2 = 0.5$) do not show significant differences compared with a Maxwell rheology (not shown). The choice of the fractional components is not simple, so in the absence of external information about the viscoelastic structure of the shell that likely surrounds the pressurized reservoir beneath Cordón Caulle, we use the simplest of all these rheologies, which is the Maxwell model.

4.2.3. Shell Radius and Viscosity

We implement our models with a shell radius of 1 km after Newman et al. (2001). This figure is essentially unconstrained due to the lack of subsurface seismic observations, but we note that there is an inverse trade-off between shell radius and pressure because increasing the shell radius will reduce the overpressure required to model a given uplift signal. The most critical parameter in the simulation is the shell viscosity because it controls the timescale of the viscous relaxation, but it can vary several orders of magnitude depending on the rock composition, water content, and temperature among other factors.

Newman et al. (2001) used petrological arguments and experimental models to constrain the shell viscosity given the medium thermal state and rheology underneath Long Valley caldera. These figures span 2 orders of magnitude ($\sim 10^{15}\text{--}10^{17}$ Pa·s) and agree with those derived from the time constants of exponential data fits, representative of largely crystallized rhyolites near their solidus but not of partially molten rocks. Thermal models that could be used to provide more realistic estimates of shell viscosity by means of a power law function (e.g., Del Negro et al., 2009) are not available at Cordón Caulle; hence, we use a constant shell viscosity only. Nevertheless, most of the published viscoelastic models (Table 4) have relied on either a parametric forward exploration (Pearse & Fialko, 2010) or just assuming a fixed figure (Hickey et al., 2013). Here the shell viscosity will be calculated directly from the data instead of using a fixed value.

The initial shell viscosity of the source responsible for the 2012–2015 deformation signal is calculated with a spherical shell as an initial model, even though the ground deformation signal is clearly nonsymmetric (Figure 1). The viscosity of a spherical shell of radius R_2 surrounding a spherical reservoir of radius R_1 is

$$\eta = \frac{G\tau_r(1+\nu)}{3(1-\nu)} \left(\frac{R_1}{R_2}\right)^3 \quad (4)$$

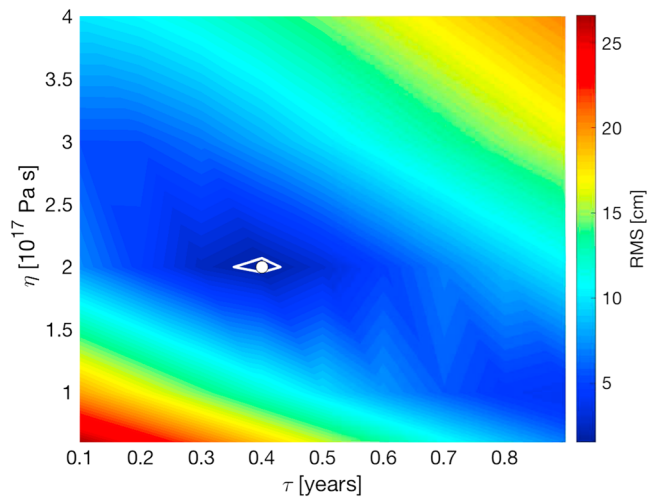


Figure 8. Root mean square (RMS) in centimeters between the March 2012 to January 2016 CSK time series (Figure 2) and the synthetic signal predicted by finite element viscoelastic models with variable shell viscosity η and pressurization timescale τ for a maximum pressure of 19 MPa. The white point shows the best fit model parameter, and the white line is the confidence interval, defined as a variation of 10% with respect to the RMS minimum.

with the relaxation time and G the shear modulus (Equation 7.98 of Segall, 2010). The result of the time series inversion for a source with a radius of 1 km and a shell radius of 2 km at a depth of ~ 7 km (Figures S7 and S8) is within the range of values valid for the Mogi model radius-to-depth ratio and can fit the CSK time series for pressurization and relaxation times of 0.175 and 1.725 years, respectively, for a maximum pressure of ~ 270 MPa. Given a shear modulus between 5 to 35 GPa, the shell viscosity varies between $1.8 \cdot 10^{16}$ and $1.3 \cdot 10^{17}$ Pa·s (Figure S8), which are within the estimates of Newman et al. (2001).

4.2.4. Viscoelastic Numerical Model With Exponentially Decreasing Pressure Function

The best fit exponential pressurization time constant and shell viscosities of the finite element simulations are sought with a grid search algorithm (Figure 8). The best fit viscoelastic model for the CSK time series has a maximum pressure of 19 MPa, a pressurization time constant of 146 days (0.4 years), and a shell viscosity of $2 \cdot 10^{17}$ Pa·s, which falls within the range of viscosities calculated with the analytic model (Equation 7.113 in Segall, 2010). The best fit viscoelastic model predicts very little deformation during 2016 (Figure 9), although it predicts less ground uplift during late 2014 to early 2015 than the actually recorded. The best fit viscoelastic model has been used to generate a set of cumulative synthetic LOS displacements that are compared to selected dates of the CSK time series (Figure S9).

5. Discussion

5.1. Magma Reservoir Pressurization With and Without Viscoelastic Relaxation

As shown in previous sections, models of magma reservoir pressurization both with and without a viscous spherical shell can model the exponential decrease in the CSK time series. The slight deviations from a linear trend during the onset of inflation in March–May 2012 (Figure 9) are similar to transient viscoelastic signals observed at the onset and end of inflation episodes in the Santorini caldera (Parks et al., 2015), although their magnitudes are of second order with respect to the main quasi-exponential or quasi-linear (Parks et al., 2015) trends. The inferred shell viscosity of $2 \cdot 10^{17}$ Pa·s is similar to that of other volcanoes (Newman et al., 2001), and the maximum source overpressure of 19 MPa is much lower than the ~ 100 MPa calculated by Delgado et al. (2016), based on incorporating both the viscous shell and the elastic layering. The source overpressure can be further decreased

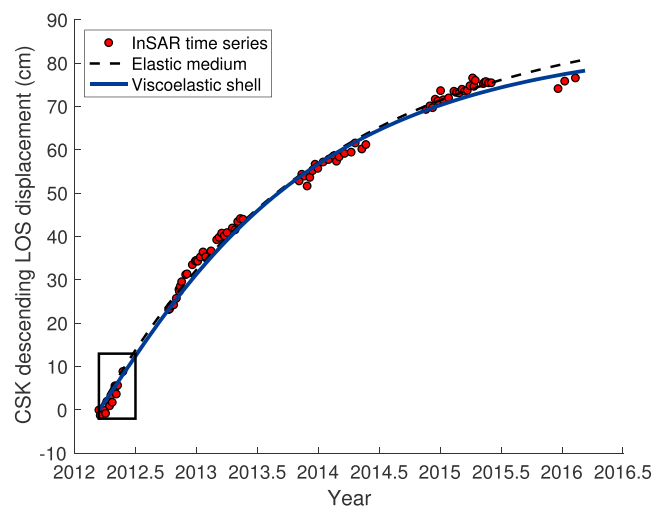


Figure 9. CSK InSAR line-of-sight (LOS) time series (red dots, Figure 2) compared with the best fit magma recharge viscoelastic and analytic models (blue and dashed black lines, respectively, Figure 5). The black dashed box shows the area where the viscoelastic model has a better data fit than the elastic one.

with a larger spheroid, but such sources are difficult to calculate because inversions for finite-sized shallow prolate spheroids are very inaccurate when the source radius of curvature is larger than its depth (Yang et al., 1988). This effect can be tested with forward finite element models where we fix the source geometry of the pressurized spheroid (Table 3) and use $b = 2.5$ and 3 km rather than 1 km. We also use $G = 20$ GPa, representative of a more brittle crust rather than the traditionally used figure of 32 GPa. This finite-sized spheroid predicts overpressures of just 8.4 and 4.7 MPa to explain the ~ 77 cm of ground uplift in the InSAR time series (Figure S10), with no need for a viscoelastic shell nor elastic layering to decrease the source overpressure. This is in agreement with other studies (Le Mével et al., 2016) and strongly suggests that viscoelastic effects are not necessary to model the InSAR data.

Although the viscoelastic model is more geologically realistic, its residuals are slightly higher than those from a purely elastic model (Figures 9, S9, and S10); hence, it does not provide an unambiguously better fit to the CSK time series than the exponential fit indicative of magma injection in an elastic medium. This is also in agreement with the constant wavelength of the ground deformation signal after the first 2.5 months of inflation, which implies no stress relaxation as in a viscoelastic simulation (Figure 6). Hence, we suggest that viscoelastic effects are of second order with respect to magma injection in an elastic medium to explain the 2012–2015 inflation at Cordón Caulle. This does not rule out the possibility that other viscoelastic simulations using more arbitrary pressurization functions that do not follow simple mathematical functions can provide a better fit to the data. However, these potential better fitting models are very difficult to find with a three-dimensional numerical simulation because every slight modification to the input pressure function results in a new model that requires many hours of calculations. It also does not imply that viscoelastic effects can be important in other systems with clear exponential ground deformation signals or that the shell viscosity is higher and viscoelastic effects might be noticeable in longer timescales of inflation (e.g., Pearse & Fialko, 2010). To our knowledge, pressure functions that do not follow simple mathematical functions (polynomial and exponential) have been tried only by the use of forward models (Hickey et al., 2016; Newman et al., 2001, 2006). It is also possible that simulations with a set of viscoelastic shells with different viscosities can explain the data (Newman et al., 2006).

The importance of viscoelastic relaxation depends on the orders of magnitude of the recharge timescale and the Maxwell relaxation time. The Maxwell relaxation time $t_R = \frac{\eta}{G}$ (Segall, 2010, equation 6.21) for $\eta = 2 \cdot 10^{17}$ Pa·s and G between 25 and 35 GPa varies between 92 and 66 days, which is significantly smaller than the best fit exponential pressurization timescale (146 days), and might explain the slight deviations from a pure exponential signal during the onset of uplift in March–May 2012 (Figure 9). However, stresses have already been relaxed during the rest of the inflation period; thus, viscoelastic effects only have a secondary effect, and the uplift signal is produced by magma recharge. It is likely that in other systems the effects of viscoelastic relaxation are more important for timescales of several years or decades, but at Cordón Caulle viscous effects are of second order compared with magma recharge in an elastic medium.

5.2. Magma Injection in a Shallow Reservoir During 2012–2018

The geodetic modeling (Figures 3 and 4) shows that the same source was active during 2012–2015 and 2016–2017. This is the first time at Cordón Caulle since the onset of high-quality geodetic measurement in January 2007 with the ALOS-1 satellite that the same source has been active in two different time periods. Euilades et al. (2017) reached this same conclusion using a prolate spheroid source model at a depth of 8 – 10 km, although the distributed sill opening model used here provides a better fit to the data. Based upon the similarity of the source model of the 2012–2015 and 2016–2017 uplift pulses (Table 2), we suggest that the latter is also due to magma injection. Also, due to the elongation of the ground deformation signal during 2016–2017 in the direction of the local volcanic chain (Figure 1), we suggest that this magma injection pulse was tectonically controlled, as has been proposed for the long-term evolution of the volcano (Lara, Lavenu, et al., 2006), and for the 2012–2015 uplift (Delgado et al., 2016). Despite the similarities of the 2012–2015 and 2016–2017 inflation events, their temporal evolution follows very different functions. The 2012–2015 inflation can be modeled by an exponential decay whereas the 2016–2017 is a linear function with some resemblance to a double exponential (Figure S11). The exponential decay implies a deep source that feeds a shallow reservoir with a constant pressure (Pinel et al., 2010), the double exponential indicates a linear pressure increase followed by a constant pressure in the deep magma source (Le Mével et al., 2016), and a linear pressure increase implies that the intrusion occurred during a much shorter timescale than the one characterized by the exponential time constant (Formula 1). The very large range of allowed magma viscosities (Figure 7) implies that it is not possible to infer the recharging magma composition in a shallow reservoir from ground

deformation data only. Unfortunately, no existing geophysical technique can image these deep structures with the required resolution (~ 10 – 100 m).

Neither the elastic nor the viscoelastic models predict both the deformation during early 2015 and the end of the inflation in May 2015, so other inelastic mechanisms are required to explain the abrupt end of magma injection. These include effects such as conduit clogging as the magma flow rate dropped because of a decrease in the pressure gradient between the shallow reservoir and a deep source (Delgado et al., 2016). A similar situation was observed during the waning of the Bárðarbunga-Holuhraun effusive eruption in Iceland, where lava extrusion ended before the prediction of exponential trends by similar coupled reservoir-conduit models (Coppola et al., 2017; Gudmundsson et al., 2016). Also, none of these coupled reservoir-conduit models can explain why the magma flow abruptly ended in February 2017 before the deformation signal either decreased or reached a value close to the asymptotic threshold as it did during 2012–2015 and why there was a time lag of ~ 1 year between the two inflation pulses. Unfortunately, existing time-dependent simulations of magma injection do not have predictive capabilities to forecast the onset and the end of ground deformation (Le Mével et al., 2016; Pinel et al., 2010; Reverso et al., 2014). Also, transient viscoelastic effects as observed at the end of the 2011–2012 inflation of Santorini (Parks et al., 2015) are not evident at the end of inflation in January and February 2017. We consider that inelastic effects such as conduit clogging due to magma solidification might be responsible for the abrupt end of uplift in February 2017, similar to the mechanism inferred for the end of the 2012–2015 inflation in May 2015.

Changes in the hydrothermal systems in silicic calderas can also explain ground deformation signals (Hurwitz et al., 2007). However, we consider that neither the 2012–2015 nor the 2016–2017 inflation can be explained by these processes because the hydrothermal system depth of ~ 2 – 3 km (Sepulveda et al., 2004, 2007) is much shallower than the inflation sources. It is possible that some of the ground deformation might be buffered by the hydrothermal system with lower shear modulus than the surrounding rock, but detailed constraints on the subsurface elastic structure are not available. Currently Cordón Caulle has neither volatiles nor gas flux monitoring, and to our knowledge its gas flux has only been measured with ground data before the 2011–2012 eruption (Sepulveda et al., 2004, 2007). Hence, the relation between the inflation events, seismicity, the degassing flux and potential changes in the volcano hydrothermal system is currently unknown. Unlike at Campi Flegrei and Yellowstone, we cannot relate the extent that seismic swarms are related to fluid injection produced by breaching of a sealed layer in the brittle-ductile transition (Hurwitz & Lowenstern, 2014). Finally, we cannot completely discard other driving mechanisms for generating the source overpressure such as H_2O exsolution in a cooling felsic crystal mush. The effect of other volatiles exsolution such as CO_2 can be discarded because their solubility is much lower than H_2O in these magmas (Tait et al., 1989). We recommend additional volatile and gas flux observations at Cordón Caulle.

In summary, volcano deformation exponential signals are inherently ambiguous to interpret, and in the absence of external information, it is difficult to discriminate between magma injection and volatile exsolution. This limitation has been observed in other large scale magmatic systems with inflation signals that last several years and where only geodetic data are available (Henderson et al., 2017; Henderson & Pritchard, 2017; Lundgren et al., 2017). One way to rule out gas exsolution produced by crystallization of anhydrous minerals with respect to magma recharge is by means of time-lapse microgravity observations (Carbone et al., 2017) that can track mass changes resulting from magma intrusion. Time-lapse microgravity data have been useful to show that uplift at Three Sisters required a significant viscoelastic response (Zurek et al., 2012), while uplift events at Laguna del Maule (Miller, Le Mevel, et al., 2017), Yellowstone (Tizzani et al., 2015), and Long Valley (Battaglia et al., 1999) have been produced by magma injection, although a recent study (Hildreth, 2017) has challenged this interpretation for the latter volcano. The intrusion of 0.125 and 0.02 km³ of basalt with a density of $2,850$ kg/m³ into a spherical reservoir at a depth of 6 km produces a maximum gravity change of 66 and 10 μ Gal for the 2012–2015 and 2016–2017 inflation events, respectively. The former signal should be detectable, while the latter is within the uncertainty of time-lapse surveys (Williams-Jones & Rymer, 2002), unless magma is intruded at a much shallower depth of 3 km, increasing the gravity change to 40 μ Gal. Despite the small predicted gravity changes, microgravity measurements can shed light on the driving mechanism of uplift events at Cordón Caulle and reduce the inherent ambiguity in the interpretation of ground deformation data. Therefore, we recommend additional microgravity measurements at Cordón Caulle.

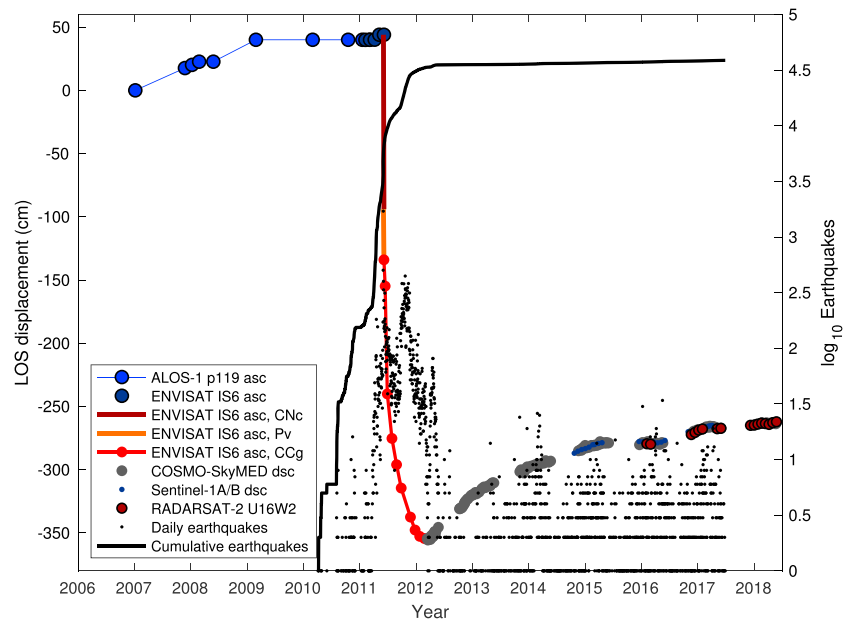


Figure 10. Compilation of selected InSAR time series between January 2007 and March 2018 (Delgado et al., 2016; Jay et al., 2014; this study) from the ALOS-1, ENVISAT, CSK, and Sentinel-1 satellites; asc and dsc are ascending and descending data, respectively. Volcanotectonic and long-period earthquakes are shown as daily and cumulative sums between April 2010 and June 2017 on a logarithmic scale (Wendt et al., 2017) and updated from the OVDAS-SERNAGEOMIN data catalog. The ALOS-1 path 119 (p119) time series shows the maximum ground uplift compiled from individual interferograms (Jay et al., 2014). The ENVISAT data are from the IS6 beam and is presented with different colors because it records deformation from four deformation sources: preeruptive in the Cordón Caulle graben (dark blue dots) and coeruptive deflation at Puyehue volcano (Pv, orange line), Cordillera Nevada caldera (CNC, brown line) and the Cordón Caulle graben (CCg, red line, calculated with a finite element spheroid model with the data of Jay et al., 2014). The preeruptive ALOS-1 and ENVISAT data show three pulses of ground uplift (Jay et al., 2014).

5.3. Relation Between Deformation and Seismicity

An intriguing feature of the 2012–2015 and 2016–2017 inflation events is the overall lack of abnormal seismicity (Delgado et al., 2016). The only abnormal seismicity since the onset of inflation in March 2012 occurred in April 2012 (Figure 11, Delgado et al., 2016), in June 08 2016 with a maximum local magnitude M_L of 3.0 (OVDAS, 2016), which could be related to the onset of the second inflation event in June–July 2016, and in early June 2018 (OVDAS, 2018; Figure 10). A similar situation has also been observed at Long Valley caldera where only some of the seismicity is correlated with inflation events in its resurgent dome (Montgomery-Brown et al., 2015), but it is different from other systems like Yellowstone where cycles of inflation-deflation are correlated with seismic swarms (Hurwitz & Lowenstern, 2014). We speculate that the Kaiser effect (Heimisson et al., 2015) is an explanation for the overall lack of abnormal seismicity in the three posteruptive inflation events. The Kaiser effect predicts that the seismicity rate remains low until the pressurization in the magma reservoir is larger than the maximum of previous stressing cycles. Testing this hypothesis requires both geodetic and seismic data recorded in several unrest episodes like at Krafla caldera in Iceland (Heimisson et al., 2015), but such dense records are not available at Cordón Caulle.

Before 2010 the sparse volcano seismic network recorded an increase in the seismicity between June 2007 and January 2008 (Wendt et al., 2017), coincident with ~20 cm of uplift during 2007–2008 (Jay et al., 2014). However, detailed earthquake statistics are only available after April 2010 (Figure 10). Because the volcano has continuous GPS measurements only since November 2017 (Figure 2), all the available measurements of magma injection rely upon InSAR data that have been acquired since 1996, although with very poor quality observations before the start of ALOS-1 acquisitions in early 2007 (de Ruyt, 2013; Fournier et al., 2010; Jay et al., 2014; Pritchard & Simons, 2004). Hence, the lack of instrumental records before 1996 precludes testing the Kaiser effect hypothesis. Continuous acquisition of geodetic, seismic, and geochemical data during future uplift pulses of uplift will help to further clarify this point.

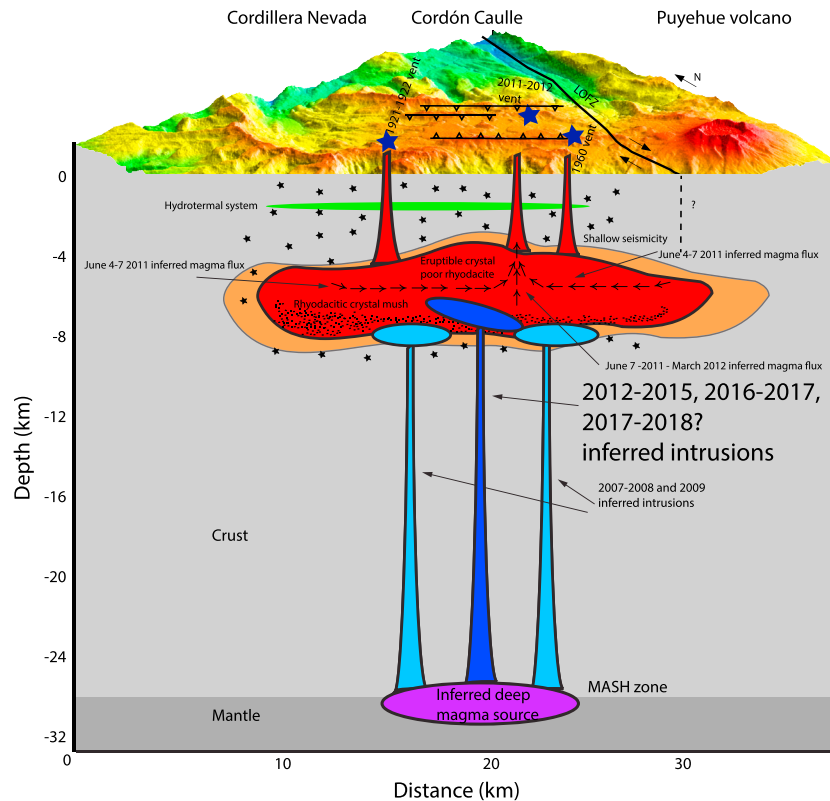


Figure 11. Cordón Caulle conceptual geological cross section (updated from Delgado et al., 2016) that summarizes the estimated deformation sources between 2007–2012 (Jay et al., 2014), 2012–2016 (Delgado et al., 2016), and 2016–2017 (this study) derived from InSAR modeling and the inferred magma sources of the 1921–1922, 1960, and 2011–2012 eruptions from geological mapping (Castro et al., 2013; Jay et al., 2014; Lara, Moreno, et al., 2006; Singer et al., 2008). The red region is the hypothetical mush zone (which could be a collection of discrete, connected reservoirs instead of a large, interconnected zone), likely surrounded by a viscoelastic shell (orange region). The light blue and blue regions are the inferred magma intrusions for 2007–2008, 2009, 2012–2015, 2016–2017, and potentially during 2017–2018, and the green region is the hydrothermal system beneath the volcano (Sepulveda et al., 2004, 2007). Blue stars show the location of the historical eruptive vents, black stars are earthquakes beneath the volcano (Delgado et al., 2016; Wendt et al., 2017), horizontal lines with open triangles show the graben bounding faults, and LOFZ is the Liquiñe-Ofqui regional fault zone that crosses the volcano (Lara, Lavenu, et al., 2006). MASH zone refers to a hypothetical zone of magma melting, assimilation, storage, and homogenization (Hildreth & Moorbath, 1988) that we infer to be the source of magmas (see rationale in Jay et al., 2014). Black points in the red regions show crystals that might have settled at the bottom of the reservoir, thus reducing the magma viscosity (Castro et al., 2013) and enhancing interstitial liquid extraction, a condition likely required to produce eruptible magma in a silicic magma chamber (Bachmann & Bergantz, 2008; Cooper, 2017). The sketch shows that the source of the 1921–1922, 1960, and 2011–2012 eruptions is the same reservoir located beneath Cordillera Nevada, Cordón Caulle, and Puyehue volcanoes and where magma intruded during 2007–2008, 2008–2009, 2012–2015, 2016–2017, and potentially during 2017–2018. InSAR data are interpreted to show that magma flowed from the Cordillera Nevada and Puyehue volcanoes toward the 2011–2012 eruptive event during the first three eruption days and then flowed from areas closer to the vent during the rest of the eruption (Jay et al., 2014). Note that the shape of the crystal mush is hypothetical because no seismic tomography is available for the volcano.

5.4. Evidence for Geodetically Detected Crystal Mush Rejuvenation Events

As currently understood, magma reservoirs underlying silicic systems are made up of crystal mushes, which are semirigid sponges of crystals (>40–50%) with small fractions of melt (Bachmann & Bergantz, 2008; Cooper, 2017; Hildreth, 2004). Crystals spend most of their lifetimes in these mushes under cold storage conditions (Cooper & Kent, 2014) because large magmatic systems are likely ephemeral (Cashman et al., 2017). Radiometric ages suggest that these mushes are rejuvenated by discrete and ephemeral intrusions of magma batches that provide the heat and volatiles that prevent the thermomechanical locking of the mush and can eventually trigger an eruption. The intrusion timescales are several decades to centuries (Bachmann & Huber, 2016) inferred from either zircon geochronology (Cooper, 2017) or diffusion modeling in zoned crystals (Costa & Dungan, 2005). Alternative views on silicic reservoirs suggest that these discrete events do not provide

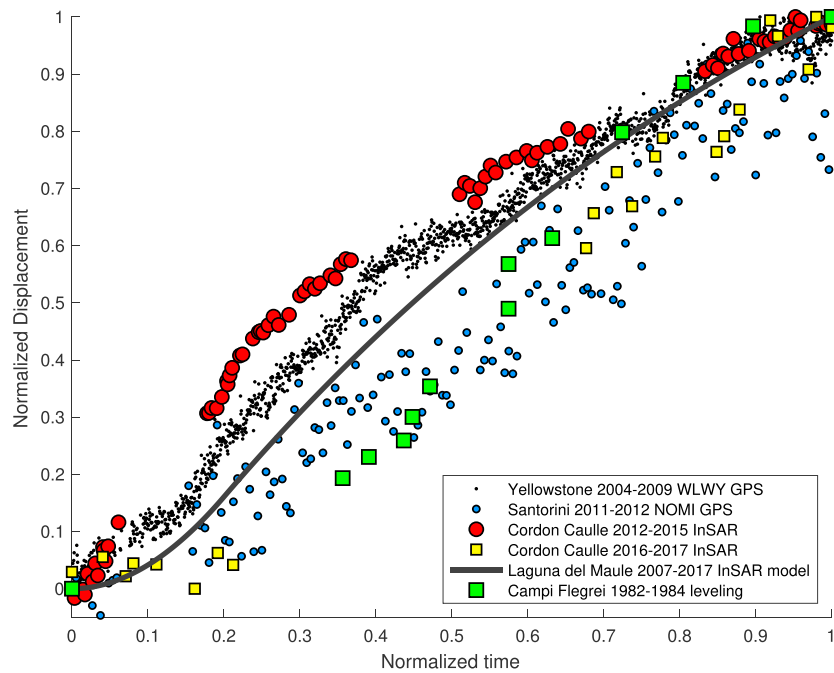


Figure 12. Time series of normalized ground deformation at silicic volcanoes. The compilation includes both meter scale signals like at Laguna del Maule and signals with amplitudes of 10–20 cm as in Santorini. The data were normalized by dividing by the maximum displacement and the total duration of each inflation event. The InSAR time series are plotted for the points of maximum displacement. Data sources: Yellowstone (Chang et al., 2010), Santorini (Newman et al., 2012), Cordón Caulle (Delgado et al., 2016; this study), Laguna del Maule (Le Mével et al., 2016), and Campi Flegrei (Battaglia et al., 1999). The Yellowstone and Santorini data sets are GPS vertical displacements from the WLWY and NOMI stations, respectively, and processed by the Nevada Geodetic Laboratory. Data from Long Valley caldera (Montgomery-Brown et al., 2015) have not been included because the uplift signals recorded since the mid-1970s have been recently reinterpreted as being produced by volatile exsolution rather than magma injection (Hildreth, 2017). The 2004–2009 Yellowstone inflation resembles a similar concave function, but it displays a convex shape at the onset of the inflation produced by a short-lived increase in the pressure in a deep source.

enough source overpressure above the tensile strength of the wall rock; hence, other mechanisms such as volatile exsolution must occur in order to trigger an eruption (Putirka, 2017). The much shorter temporal sampling of geodesy makes it a useful tool to resolve mush rejuvenation events that occur on short timescales of just a few months.

We speculate that the underlying system beneath Cordón Caulle is a crystal mush given the petrological and geochemical similarities of the erupted rhyolites in the 1921–1922, 1960, and 2011–2012 eruptions that are thought to be fed from the same reservoir (Castro et al., 2013; Jay et al., 2014; Figure 11). To test this hypothesis requires additional data sets that are currently unavailable, such as detailed zircon geochronology studies of these rhyodacitic lava flows and high-resolution geophysical imaging of the volcano subsurface. The source volumetric changes from geodetic inversions before and after the eruption are ~ 0.01 – 0.04 km³/year (Delgado et al., 2016; Jay et al., 2014), ~ 1 – 2 orders of magnitude larger than the volcano average extrusion rate during the past 300 Kyr (Singer et al., 2008), and the average growth rate of plutons in the upper crust (Annen, 2009; Menand et al., 2015). Thus, we propose that the crystal mush underlying Cordón Caulle is rejuvenated by transient and short-lived episodes of magma recharge that could last only a few months as in 2016–2017. Nonetheless, the 2016–2017 uplift did not trigger an eruption because its source pressure change was ~ 1 – 2 orders of magnitude below the tensile strength of the rocks as predicted by a simple rupture criteria (Browning et al., 2015). The chemical composition of the intruding magma cannot be constrained from geodetic data only, and it is not known how many injection events are required to trigger an eruption. Nevertheless, numerical models applied to the 2011–2012 unrest episode of Santorini caldera show that they must be larger and last longer than a given threshold, which is a function of the magma properties and plumbing system (Degruyter et al., 2016). Within the framework of this model, the 2012–2015 inflation is interpreted as the refilling of the crystal mush that deflated during the 2011–2012 eruption. More realistic models of

crystal mush rejuvenation due to episodic magma recharge should couple ground deformation and seismic data, the crust response due to reservoir pressurization, conduit flow from a deeper source, and the fluid dynamics and chemical evolution of the reservoir, although these models are very complex and yet to be completed (Bachmann & Huber, 2016).

5.5. Meter Scale Displacement in Silicic Volcanoes

Aside from Cordón Caulle, only a few other silicic systems have similar instrumentally recorded meter scale inflation and deflation cycles with nonlinear trends. These include the restless Campi Flegrei, Rabaul, and Long Valley calderas (Battaglia et al., 1999; Montgomery-Brown et al., 2015), and the Laguna del Maule volcanic complex (Le Mével et al., 2015, 2016; Singer et al., 2018). Although Cordón Caulle is not a caldera, its geodetic time series resemble those of restless silicic caldera scale systems (Figure 12), with multiple inflation events in several decades (Biggs & Pritchard, 2017). Uplift signals in calderas tend to display an increase in the uplift rate followed by either decreased or constant rates, which can be explained by a double exponential model in which the pressure from a deep source increases linearly and then becomes constant (Le Mével et al., 2015, 2016). This double exponential model shows time series with a characteristic convex-concave shape, while post-eruptive inflation signals tend to be concave because they only display a single exponential decay. The temporal trend of the 2016–2017 inflation lies within the framework of this double exponential model (Figure S11), as could the poorly constrained 2007–2011 inflation pulses. On the contrary, the exponential signal recorded during 2012–2015 is a post-eruptive reservoir refill pulse with a concave shape only, different from the uplift signals observed in other silicic systems, and indicative of no pressure increase in the deep magma source (Figure 12). Despite the similarity of the deformation trends, this does not imply that Cordón Caulle is a caldera nor that its plumbing system is caldera sized. For example, the Laguna del Maule rhyolitic volcanic complex has inflated more than 2.5 m in ~10 years (Le Mével et al., 2015; Singer et al., 2018), albeit with a different temporal pattern and with a plumbing system of only ~30 km³ (Miller, Williams-Jones, et al., 2017). The actual dimensions of the Cordón Caulle plumbing system are unknown as no detailed geophysical imaging has been carried out, but it is likely that it is larger than 30 km³ based on the size of the prolate spheroid source model for the 2012–2015 inflation ($V_{\text{spheroid}} = \frac{4\pi}{3}ab^2 = \sim 30 \text{ km}^3$, Table 3).

6. Conclusions

In this study we have presented InSAR time series at Cordón Caulle volcano that show a second and potential third pulse of post-eruptive inflation in 2016–2017 and 2017–2018, respectively, following the 2011–2012 silicic eruption and the 2012–2015 subsequent inflation. The 2012–2018 uplift cycle with a total inflation of ~0.9 m is unique at Cordón Caulle because it is the first time since the onset of high-quality geodetic measurements in 2007 that the same magma reservoir has been active twice. The best fit model of these ground deformation pulses is a sill at a depth of ~6 km and elongated in the direction of the volcano. Numerical models of ground deformation for a viscoelastic shell ($\eta = 2 \cdot 10^{17} \text{ Pa}\cdot\text{s}$) that surrounds a pressurized reservoir do not provide a better data fit to the exponential inflation signal during 2012–2015 than a simple elastic model of magma recharge. Hence, viscoelastic effects are negligible for the 2012–2015 inflation and the uplift is most likely due to magma injection. The temporal evolution of the uplift and the similarity in the source geometry suggests that both the 2012–2015 and 2016–2017 inflation pulses were produced by magma injection in the crystal mush that likely underlies the volcano, both of which were associated with low seismicity levels. Between January 2007 and May 2018, the volcano showed a complex cycle of five transient pulses of meter scale inflation that resemble sequences of magma injection in caldera scale systems elsewhere. The short duration of geodetically detected inflation pulses in the crystal mush that likely underlies Cordón Caulle suggest that they have timescales of several months, much shorter than the decades to hundreds of years inferred from radiometric ages. Given the meter scale of inflation at Cordón Caulle, we suggest a continuous multiparametric monitoring strategy (gas, temperature, microgravity, and seismicity), and physicochemical numerical modeling in addition to the continuous stream of data recorded by the civilian SAR constellation,

References

- Aagaard, B. T., Knepley, M. G., & Williams, C. A. (2013). A domain decomposition approach to implementing fault slip in finite-element models of quasi-static and dynamic crustal deformation. *Journal of Geophysical Research: Solid Earth*, *118*, 3059–3079. <https://doi.org/10.1002/jgrb.50217>
- Agram, P. S., Jolivet, R., Riel, B., Lin, Y. N., Simons, M., Hetland, E., et al. (2013). New radar interferometric time series analysis toolbox released. *Eos, Transactions American Geophysical Union*, *94*(7), 69–70. <https://doi.org/10.1002/2013EO070001>
- Amoruso, A., & Crescentini, L. (2009). Shape and volume change of pressurized ellipsoidal cavities from deformation and seismic data. *Journal of Geophysical Research*, *114*, B02210. <https://doi.org/10.1029/2008JB005946>

Acknowledgments

This project is part of the CEOS Volcano pilot program coordinated by Michael Poland (USGS) and Simona Zoffoli (ASI). F. D. and M. E. P. were partially supported by NASA's Science Mission Directorate grants NNX12AM24G and NNX16AK87G. F. D. acknowledges CONICYT-Becas Chile for a PhD scholarship and NASA for the Earth and Space Sciences Fellowship. COSMO-SkyMED data were provided by Agenzia Spaziale Italiana (ASI). RADARSAT-2 data were provided by the Canadian Space Agency (CSA); MacDonald, Dettwiler & Associates (MDA) Ltd., and the SOAR-EI project #5437 *InSAR-detected magma recharge in silicic volcanoes*. Sentinel-1A/B data were provided by the European Space Agency (ESA) and distributed by the Alaska Satellite Facility (ASF). ALOS-2 data were provided by the Japanese Aerospace Exploration Agency (JAXA) through the CEOS pilot project and by a JAXA RA6 grant to collaborator Paul Lundgren (Jet Propulsion Laboratory, JPL). The ALOS-2 SM3 time series was processed at JPL during a research visit of F. D. to this institution. We thank Centro Sismológico Nacional (CSN) for providing the data of the GNSS station PAJA; Pablo Euillades (Universidad Nacional de Cuyo) and Hélène Le Mével (Carnegie Institution for Science) for sharing the time series used in Figures 2 and 12; Daniel Basualto (OVDAS) and OVDAS- SERNAGEOMIN for providing the seismicity catalog and the GPS data; Paul Lundgren (JPL) for sharing ALOS-2 data and useful discussions; Kyle Anderson (USGS) for discussions on dynamic models of magma injection; and Eric Fielding (JPL) for providing prototype additions for processing zero-doppler single look complex (SLC) data. We also acknowledge Editor Michael Walter, Associate Editor Michael Poland, Paul Lundgren, and an anonymous reviewer for their comments that improved the quality of this manuscript. Several figures were created with the GMT software (Wessel & Smith, 1998). Sentinel-1 SLC images are freely available for download at ASF. The CSK time series used in Figure 9 for the viscoelastic simulations is available for download at zenodo.org. The processed data sets and intermediate products are available upon request to the authors.

- Annen, C. (2009). From plutons to magma chambers: Thermal constraints on the accumulation of eruptible silicic magma in the upper crust. *Earth and Planetary Science Letters*, 284(3-4), 409–416. <https://doi.org/10.1016/j.epsl.2009.05.006>
- Bachmann, O., & Bergantz, G. (2008). The magma reservoirs that feed supereruptions. *Elements*, 4(1), 17–21. <https://doi.org/10.2113/gselements.4.1.17>
- Bachmann, O., & Huber, C. (2016). Silicic magma reservoirs in the Earth's crust. *American Mineralogist*, 101(11), 2377–2404. <https://doi.org/10.2138/am-2016-5675>
- Bagnardi, M., & Amelung, F. (2012). Space-geodetic evidence for multiple magma reservoirs and subvolcanic lateral intrusions at Fernandina Volcano, Galapagos Islands. *Journal of Geophysical Research*, 117, B10406. <https://doi.org/10.1029/2012JB009465>
- Bato, M. G., Pinel, V., Yan, Y., Jouanne, F., & Vandemeulebrouck, J. (2018). Possible deep connection between volcanic systems evidenced by sequential assimilation of geodetic data. *Scientific Reports*, 8(1), 11702. <https://doi.org/10.1038/s41598-018-29811-x>
- Battaglia, M., Roberts, C., & Segall, P. (1999). Magma intrusion beneath Long Valley caldera confirmed by temporal changes in gravity. *Science*, 285(5436), 2119–2122. <https://doi.org/10.1126/science.285.5436.2119>
- Biggs, J., & Pritchard, M. E. (2017). Global volcano monitoring: What does it mean when volcanoes deform? *Elements*, 13(1), 17–22. <https://doi.org/10.2113/gselements.13.1.17>
- Bonafede, M., Dragoni, M., & Quarenzi, F. (1986). Displacement and stress fields produced by a centre of dilation and by a pressure source in a viscoelastic half-space: Application to the study of ground deformation and seismic activity at Campi Flegrei, Italy. *Geophysical Journal International*, 87(2), 455–485. <https://doi.org/10.1111/j.1365-246X.1986.tb06632.x>
- Browning, J., Drymoni, K., & Gudmundsson, A. (2015). Forecasting magma-chamber rupture at Santorini volcano, Greece. *Scientific Reports*, 5, 15785. <https://doi.org/10.1038/srep15785>
- Carbone, D., Poland, M. P., Diamant, M., & Greco, F. (2017). The added value of time-variable microgravimetry to the understanding of how volcanoes work. *Earth-Science Reviews*, 169, 146–179. <https://doi.org/10.1016/j.earscirev.2017.04.014>
- Cashman, K. V., Sparks, R. S. J., & Blundy, J. D. (2017). Vertically extensive and unstable magmatic systems: A unified view of igneous processes. *Science*, 355, eaag3055. <https://doi.org/10.1126/science.aag3055>
- Castro, J. M., Cordonnier, B., Schipper, C. I., Tuffen, H., Baumann, T. S., & Feisel, Y. (2016). Rapid laccolith intrusion driven by explosive volcanic eruption. *Nature Communications*, 7, 13585. <https://doi.org/10.1038/ncomms13585>
- Castro, J. M., Schipper, C. I., Mueller, S. P., Militzer, A. S., Amigo, A., Parejas, C. S., & Jacob, D. (2013). Storage and eruption of near-liquidus rhyolite magma at Cordón Caulle, Chile. *Bulletin of Volcanology*, 75(4), 1–17. <https://doi.org/10.1007/s00445-013-0702-9>
- Chadwick, W. W., Nooner, S. L., Butterfield, D. A., & Lilley, M. D. (2012). Seafloor deformation and forecasts of the April 2011 eruption at Axial Seamount. *Nature Geoscience*, 5(7), 474–477. <https://doi.org/10.1038/ngeo1464>
- Chang, W.-L., Smith, R. B., Farrell, J., & Puskas, C. M. (2010). An extraordinary episode of Yellowstone caldera uplift, 2004–2010, from GPS and InSAR observations. *Geophysical Research Letters*, 37, L23302. <https://doi.org/10.1029/2010GL045451>
- Chen, C. W., & Zebker, H. A. (2001). Two-dimensional phase unwrapping with use of statistical models for cost functions in nonlinear optimization. *Journal of the Optical Society of America a-Optics Image Science and Vision*, 18(2), 338–351. <https://doi.org/10.1364/josaa.18.000338>
- Cooper, K. M. (2017). What does a magma reservoir look like? the “Crystal’s-Eye” view. *Elements*, 13(1), 23–28. <https://doi.org/10.2113/gselements.13.1.23>
- Cooper, K. M., & Kent, A. J. (2014). Rapid remobilization of magmatic crystals kept in cold storage. *Nature*, 506, 480–483. <https://doi.org/10.1038/nature12991>
- Coppola, D., Ripepe, M., Laiolo, M., & Cigolini, C. (2017). Modelling satellite-derived magma discharge to explain caldera collapse. *Geology*, 45(6), 523–526. <https://doi.org/10.1130/g38866.1>
- Costa, F., & Dungan, M. (2005). Short time scales of magmatic assimilation from diffusion modeling of multiple elements in olivine. *Geology*, 33(10), 837–840. <https://doi.org/10.1130/g21675.1>
- de Ruyt, R. (2013). Análisis comparativo de las técnicas de InSAR persistent scatterers interferometry (PSI) y small baseline subset (SBAS) aplicadas en la medición de deformaciones del complejo volcánico Cordón Caulle (40.55) — Andes Del Sur (Ph.D. thesis), Cordoba.
- Degruyter, W., Huber, C., Bachmann, O., Cooper, K. M., & Kent, A. J. R. (2016). Magma reservoir response to transient recharge events: The case of Santorini volcano (Greece). *Geology*, 44(1), 23–26. <https://doi.org/10.1130/g37333.1>
- Del Negro, C., Currenti, G., & Scandura, D. (2009). Temperature-dependent viscoelastic modeling of ground deformation: Application to Etna volcano during the 1993–1997 inflation period. *Physics of the Earth and Planetary Interiors*, 172(3-4), 299–309. <https://doi.org/10.1016/j.pepi.2008.10.019>
- Delgado, F., Pritchard, M. E., Basualto, D., Lazo, J., Cordova, L., & Lara, L. E. (2016). Rapid reinflation following the 2011–2012 rhyodacite eruption at Cordon Caulle volcano (Southern Andes) imaged by InSAR: Evidence for magma reservoir refill. *Geophysical Research Letters*, 43, 9552–9562. <https://doi.org/10.1002/2016GL070066>
- Delgado, F., Pritchard, M., Ebemier, S., Gonzalez, P., & Lara, L. (2017). Recent unrest (2002–2015) imaged by space geodesy at the highest risk Chilean volcanoes: Villarrica, Llaima, and Calbuco (Southern Andes). *Journal of Volcanology and Geothermal Research*, 344, 270–288. <https://doi.org/10.1016/j.jvolgeores.2017.05.020>
- Dragoni, M., & Magnanensi, C. (1989). Displacement and stress produced by a pressurized, spherical magma chamber, surrounded by a viscoelastic shell. *Physics of the Earth and Planetary Interiors*, 56(3-4), 316–328. [https://doi.org/10.1016/0031-9201\(89\)90166-0](https://doi.org/10.1016/0031-9201(89)90166-0)
- Dvorak, J. J., & Okamura, A. T. (1987). A hydraulic model to explain variations in summit tilt rate at Kilauea and Mauna-Loa Volcanoes, *Volcanism in Hawaii* (Vol. 1350, pp. 1281–1296). Reston, Virginia: U. S. Geol. Surv. Prof. Pap.
- Dzurisin, D., Lisowski, M., & Wicks, C. W. (2009). Continuing inflation at Three Sisters volcanic center, central Oregon Cascade Range, USA, from GPS, leveling, and InSAR observations. *Bulletin of Volcanology*, 71(10), 1091–1110. <https://doi.org/10.1007/s00445-009-0296-4>
- Euillades, P. A., Euillades, L. D., Blanco, M. H., Velez, M. L., Grosse, P., & Sosa, G. J. (2017). Co-eruptive subsidence and post-eruptive uplift associated with the 2011–2012 eruption of Puyehue-Cordón Caulle, Chile, revealed by DInSAR. *Journal of Volcanology and Geothermal Research*, 344, 257–269. <https://doi.org/10.1016/j.jvolgeores.2017.06.023>
- Farr, T. G., Rosen, P. A., Caro, E., Crippen, R., Duren, R., Hensley, S., et al. (2007). The shuttle radar topography mission. *Reviews of Geophysics*, 45, RG2004. <https://doi.org/10.1029/2005RG000183>
- Fattahi, H., Agram, P., & Simons, M. (2017). A network-based enhanced spectral diversity approach for TOPS time-series analysis. *IEEE Transactions on Geoscience and Remote Sensing*, 55(2), 777–786. <https://doi.org/10.1109/TGRS.2016.2614925>
- Fattahi, H., & Amelung, F. (2013). DEM error correction in InSAR time series. *IEEE Transactions on Geoscience and Remote Sensing*, 51(7), 4249–4259. <https://doi.org/10.1109/tgrs.2012.2227761>
- Fialko, Y., & Pearce, J. (2012). Sombbrero uplift above the Altiplano-Puna magma body: Evidence of a ballooning mid-crustal diapir. *Science*, 338(6104), 250–252. <https://doi.org/10.1126/science.1226358>

- Finnegan, N. J., Pritchard, M. E., Lohman, R. B., & Lundgren, P. R. (2008). Constraints on surface deformation in the Seattle, WA, urban corridor from satellite radar interferometry time-series analysis. *Geophysical Journal International*, *174*(1), 29–41. <https://doi.org/10.1111/j.1365-246X.2008.03822.x>
- Fournier, T. J., Pritchard, M. E., & Riddick, S. N. (2010). Duration, magnitude, and frequency of subaerial volcano deformation events: New results from Latin America using InSAR and a global synthesis. *Geochemistry, Geophysics, Geosystems*, *11*, Q01003. <https://doi.org/10.1029/2009GC002558>
- Freed, A. M., & Burgmann, R. (2004). Evidence of power-law flow in the Mojave desert mantle. *Nature*, *430*(6999), 548–551. <https://doi.org/10.1038/nature02784>
- Fukushima, Y., Cayol, V., Durand, P., & Massonnet, D. (2010). Evolution of magma conduits during the 1998–2000 eruptions of Piton de la Fournaise volcano, Reunion Island. *Journal of Geophysical Research*, *115*, B10204. <https://doi.org/10.1029/2009JB007023>
- Galgana, G. A., Newman, A. V., Hamburger, M. W., & Solidum, R. U. (2014). Geodetic observations and modeling of time-varying deformation at Taal Volcano, Philippines. *Journal of Volcanology and Geothermal Research*, *271*, 11–23. <https://doi.org/10.1016/j.jvolgeores.2013.11.005>
- Goldstein, R. M., & Werner, C. L. (1998). Radar interferogram filtering for geophysical applications. *Geophysical Research Letters*, *25*(21), 4035–4038. <https://doi.org/10.1029/1998GL900033>
- Gottsmann, J., Blundy, J., Henderson, S., Pritchard, M. E., & Sparks, R. S. J. (2017). Thermomechanical modeling of the Altiplano-Puna deformation anomaly: Multiparameter insights into magma mush reorganization. *Geosphere*, *13*(4), 1042–1065. <https://doi.org/10.1130/GES01420.1>
- Gottsmann, J., & Odbert, H. (2014). The effects of thermomechanical heterogeneities in island arc crust on time-dependent preruptive stresses and the failure of an andesitic reservoir. *Journal of Geophysical Research: Solid Earth*, *119*, 4626–4639. <https://doi.org/10.1002/2014JB011079>
- Gregg, P. M., de Silva, S. L., & Grosfils, E. B. (2013). Thermomechanics of shallow magma chamber pressurization: Implications for the assessment of ground deformation data at active volcanoes. *Earth and Planetary Science Letters*, *384*, 100–108. <https://doi.org/10.1016/j.epsl.2013.09.040>
- Gudmundsson, M. T., Jonsdottir, K., Hooper, A., Holohan, E. P., Halldorsson, S. A., Ofeigsson, B. G., et al. (2016). Gradual caldera collapse at Bárðarbunga volcano, Iceland, regulated by lateral magma outflow. *Science*, *353*(6296), aaf8988. <https://doi.org/10.1126/science.aaf8988>
- Heimisson, E. R., Einarsson, P., Sigmundsson, F., & Brandsdottir, B. (2015). Kilometer-scale Kaiser effect identified in Krafla volcano, Iceland. *Geophysical Research Letters*, *42*, 7958–7965. <https://doi.org/10.1002/2015GL065680>
- Henderson, S. T., Delgado, F., Elliott, J., Pritchard, M. E., & Lundgren, P. R. (2017). Decelerating uplift at Lazufre volcanic center, Central Andes, from A.D. 2010 to 2016, and implications for geodetic models. *Geosphere*, *13*, 1489–1505. <https://doi.org/10.1130/GES01441.1>
- Henderson, S. T., & Pritchard, M. E. (2017). Time-dependent deformation of Uturuncu Volcano, Bolivia, constrained by GPS and InSAR measurements and implications for source models. *Geosphere*, *13*, 1834–1854. <https://doi.org/10.1130/GES01203.1>
- Hickey, J., Gottsmann, J., & del Potro, R. (2013). The large-scale surface uplift in the Altiplano-Puna region of Bolivia: A parametric study of source characteristics and crustal rheology using finite element analysis. *Geochemistry, Geophysics, Geosystems*, *14*, 540–555. <https://doi.org/10.1002/ggge.20057>
- Hickey, J., Gottsmann, J., & Mothes, P. (2015). Estimating volcanic deformation source parameters with a finite element inversion: The 2001–2002 unrest at Cotopaxi volcano, Ecuador. *Journal of Geophysical Research: Solid Earth*, *120*, 1473–1486. <https://doi.org/10.1002/2014JB011731>
- Hickey, J., Gottsmann, J., Nakamichi, H., & Iguchi, M. (2016). Thermomechanical controls on magma supply and volcanic deformation: Application to Aira caldera, Japan. *Scientific Reports*, *6*, 32691. <https://doi.org/10.1038/srep32691>
- Hildreth, W. (2004). Volcanological perspectives on Long Valley, Mammoth Mountain, and Mono Craters: Several contiguous but discrete systems. *Journal of Volcanology and Geothermal Research*, *136*(3–4), 169–198. <https://doi.org/10.1016/j.jvolgeores.2004.05.019>
- Hildreth, W. (2017). Fluid-driven uplift at Long Valley Caldera, California: Geologic perspectives. *Journal of Volcanology and Geothermal Research*, *341*, 269–286. <https://doi.org/10.1016/j.jvolgeores.2017.06.010>
- Hildreth, W., & Moorbath, S. (1988). Crustal contributions to arc magmatism in the Andes of Central Chile. *Contributions to Mineralogy and Petrology*, *98*(4), 455–489. <https://doi.org/10.1007/bf00372365>
- Hurwitz, S., Christiansen, L. B., & Hsieh, P. A. (2007). Hydrothermal fluid flow and deformation in large calderas: Inferences from numerical simulations. *Journal of Geophysical Research*, *112*, B02206. <https://doi.org/10.1029/2006JB004689>
- Hurwitz, S., & Lowenstern, J. B. (2014). Dynamics of the Yellowstone hydrothermal system. *Reviews of Geophysics*, *52*, 375–411. <https://doi.org/10.1002/2014RG000452>
- Jay, J., Costa, F., Pritchard, M., Lara, L., Singer, B., & Herrin, J. (2014). Locating magma reservoirs using InSAR and petrology before and during the 2011–2012 Cordon Caulle silicic eruption. *Earth and Planetary Science Letters*, *395*, 254–266. <https://doi.org/10.1016/j.epsl.2014.03.046>
- Lara, L. E., Lavenu, A., Cembrano, J., & Rodriguez, C. (2006). Structural controls of volcanism in transversal chains: Resheared faults and neotectonics in the Cordon Caulle-Puyehue area (40.5 degrees S), Southern Andes. *Journal of Volcanology and Geothermal Research*, *158*(1–2), 70–86. <https://doi.org/10.1016/j.jvolgeores.2006.04.017>
- Lara, L. E., Moreno, H., Naranjo, J. A., Matthews, S., & de Arce, C. P. (2006). Magmatic evolution of the Puyehue-Cordon Caulle volcanic complex (40 degrees S), Southern Andean Volcanic Zone: From shield to unusual rhyolitic fissure volcanism. *Journal of Volcanology and Geothermal Research*, *157*(4), 343–366. <https://doi.org/10.1016/j.jvolgeores.2006.04.010>
- Le Mével, H., Feigl, K. L., Córdova, L., DeMets, C., & Lundgren, P. (2015). Lundgren evolution of unrest at Laguna del Maule volcanic field (Chile) from InSAR and GPS measurements, 2003 to 2014. *Geophysical Research Letters*, *42*, 6590–6598. <https://doi.org/10.1002/2015GL064665>
- Le Mével, H., Gregg, P., & Feigl, K. L. (2016). Magma injection into a long-lived reservoir to explain geodetically measured uplift: Application to the 2007–2014 unrest episode at Laguna Del Maule Volcanic Field Chile. *Journal of Geophysical Research: Solid Earth*, *121*, 6092–6108. <https://doi.org/10.1002/2016JB013066>
- Lengline, O., Marsan, D., Got, J. L., Pinel, V., Ferrazzini, V., & Okubo, P. G. (2008). Seismicity and deformation induced by magma accumulation at three basaltic volcanoes. *Journal of Geophysical Research*, *113*, B12305. <https://doi.org/10.1029/2008JB005937>
- Leshner, C. E., & Spera, F. J. (2015). *Thermodynamic and transport properties of silicate melts and magma*: Elsevier.
- Lohman, R. B., & Simons, M. (2005). Some thoughts on the use of InSAR data to constrain models of surface deformation: Noise structure and data downsampling. *Geochemistry, Geophysics, Geosystems*, *6*, Q01007. <https://doi.org/10.1029/2004GC000841>
- Lopez-Quiroz, P., Doin, M. P., Tupin, F., Briole, P., & Nicolas, J. M. (2009). Time series analysis of Mexico City subsidence constrained by radar interferometry. *Journal of Applied Geophysics*, *69*(1), 1–15. <https://doi.org/10.1016/j.jappgeo.2009.02.006>

- Lu, Z., Dzurisin, D., Biggs, J., Wicks, C., & McNutt, S. (2010). Ground surface deformation patterns, magma supply, and magma storage at Okmok volcano, Alaska, from InSAR analysis: 1. Interruption deformation, 1997–2008. *Journal of Geophysical Research*, *115*, B00B02. <https://doi.org/10.1029/2009JB006969>
- Lu, Z., Masterlark, T., Dzurisin, D., Rykhus, R., & Wicks, C. (2003). Magma supply dynamics at Westdahl volcano, Alaska, modeled from satellite radar interferometry. *Journal of Geophysical Research*, *108*(B7), 2354. <https://doi.org/10.1029/2002JB002311>
- Lundgren, P., Nikkhoo, M., Samsonov, S. V., Milillo, P., Gil-Cruz, F., & Lazo, J. (2017). Source model for the Copahue volcano magma plumbing system constrained by InSAR surface deformation observations. *Journal of Geophysical Research: Solid Earth*, *122*, 5729–5747. <https://doi.org/10.1002/2017JB014368>
- Masterlark, T., Haney, M., Dickinson, H., Fournier, T., & Searcy, C. (2010). Rheologic and structural controls on the deformation of Okmok volcano, Alaska: FEMs, InSAR, and ambient noise tomography. *Journal of Geophysical Research*, *115*, B02409. <https://doi.org/10.1029/2009JB006324>
- McTigue, D. F. (1987). Elastic stress and deformation near a finite spherical magma body: Resolution of the point source paradox. *Journal of Geophysical Research*, *92*(B12), 12,931–12,940. <https://doi.org/10.1029/JB092iB12p12931>
- Menand, T., Annen, C., & de Saint Blanquat, M. (2015). Rates of magma transfer in the crust: Insights into magma reservoir recharge and pluton growth. *Geology*, *43*(3), 199–202. <https://doi.org/10.1130/g36224.1>
- Miller, C. A., Le Mevel, H., Currenti, G., Williams-Jones, G., & Tikoff, B. (2017). Microgravity changes at the Laguna del Maule volcanic field: Magma-induced stress changes facilitate mass addition. *Journal of Geophysical Research: Solid Earth*, *122*, 3179–3196. <https://doi.org/10.1002/2017JB014048>
- Miller, C. A., Williams-Jones, G., Fournier, D., & Witter, J. (2017). 3D gravity inversion and thermodynamic modelling reveal properties of shallow silicic magma reservoir beneath Laguna del Maule, Chile. *Earth and Planetary Science Letters*, *459*, 14–27. <https://doi.org/10.1016/j.epsl.2016.11.007>
- Montgomery-Brown, E. K., Wicks, C. W., Cervelli, P. F., Langbein, J. O., Svarc, J. L., Shelly, D. R., et al. (2015). Renewed inflation of Long Valley Caldera, California (2011 to 2014). *Geophysical Research Letters*, *42*, 5250–5257. <https://doi.org/10.1002/2015GL064338>
- Newman, A. V., Dixon, T. H., & Gourmelen, N. (2006). A four-dimensional viscoelastic deformation model for Long Valley Caldera, California, between 1995 and 2000. *Journal of Volcanology and Geothermal Research*, *150*(1–3), 244–269. <https://doi.org/10.1016/j.jvolgeores.2005.07.017>
- Newman, A. V., Dixon, T. H., Ofoegbu, G. I., & Dixon, J. E. (2001). Geodetic and seismic constraints on recent activity at Long Valley Caldera, California: Evidence for viscoelastic rheology. *Journal of Volcanology and Geothermal Research*, *105*(3), 183–206. [https://doi.org/10.1016/S0377-0273\(00\)00255-9](https://doi.org/10.1016/S0377-0273(00)00255-9)
- Newman, A. V., Stiros, S., Feng, L., Psimoulis, P., Moschas, F., Saltogianni, V., et al. (2012). Recent geodetic unrest at Santorini Caldera, Greece. *Geophysical Research Letters*, *39*, L06309. <https://doi.org/10.1029/2012GL051286>
- Nikkhoo, M., Walter, T. R., Lundgren, P. R., & Prats-Iraola, P. (2016). Compound dislocation models (CDMs) for volcano deformation analyses. *Geophysical Journal International*, *208*, 877–894. <https://doi.org/10.1093/gji/ggw427>
- Okada, Y. (1985). Surface deformation due to shear and tensile faults in a half-space. *Bulletin of the Seismological Society of America*, *75*(4), 1135–1154.
- Parks, M. M., Moore, J. D. P., Papanikolaou, X., Biggs, J., Mather, T. A., Pyle, D. M., et al. (2015). From quiescence to unrest: 20 Years of satellite geodetic measurements at Santorini volcano, Greece. *Journal of Geophysical Research: Solid Earth*, *120*, 1309–1328. <https://doi.org/10.1002/2014JB011540>
- Pearse, J., & Fialko, Y. (2010). Mechanics of active magmatic intraplate in the Rio Grande Rift near Socorro, New Mexico. *Journal of Geophysical Research*, *115*, B07413. <https://doi.org/10.1029/2009JB006592>
- Pearse, J., & Lundgren, P. (2013). Source model of deformation at Lazufre volcanic center, central Andes, constrained by InSAR time series. *Geophysical Research Letters*, *40*, 1059–1064. <https://doi.org/10.1002/grl.50276>
- Pinel, V., Jaupart, C., & Albino, F. (2010). On the relationship between cycles of eruptive activity and growth of a volcanic edifice. *Journal of Volcanology and Geothermal Research*, *194*(4), 150–164. <https://doi.org/10.1016/j.jvolgeores.2010.05.006>
- Prats-Iraola, P., Scheiber, R., Marotti, L., Wollstadt, S., & Reigber, A. (2012). TOPS interferometry with TerraSAR-x. *IEEE Transactions on Geoscience and Remote Sensing*, *50*(8), 3179–3188. <https://doi.org/10.1109/tgrs.2011.2178247>
- Pritchard, M. E., & Simons, M. (2004). An InSAR-based survey of volcanic deformation in the southern Andes. *Geophysical Research Letters*, *31*, L15610. <https://doi.org/10.1029/2004GL020545>
- Putirka, K. D. (2017). Down the crater: Where magmas are stored and why they erupt. *Elements*, *13*(1), 11–16. <https://doi.org/10.2113/gselements.13.1.11>
- Remy, D., Chen, Y., Froger, J. L., Bonvalot, S., Cordoba, L., & Fustos, J. (2015). Revised interpretation of recent InSAR signals observed at Llaima volcano (Chile). *Geophysical Research Letters*, *42*, 3870–3879. <https://doi.org/10.1002/2015GL063872>
- Reverso, T., Vandemeulebroeck, J., Jouanne, F., Pinel, V., Villemin, T., Sturkell, E., & Bascou, P. (2014). A two-magma chamber model as a source of deformation at Grimsvotn Volcano, Iceland. *Journal of Geophysical Research: Solid Earth*, *119*, 4666–4683. <https://doi.org/10.1002/2013JB010569>
- Rosen, P. A., Gurrola, E., Sacco, G. F., & Zebker, H. (2012). The InSAR Scientific Computing Environment.
- Rubin, A. M. (1995). Propagation of magma-filled cracks. *Annual Review of Earth and Planetary Sciences*, *23*, 287–336. <https://doi.org/10.1146/annurev.ea.23.050195.001443>
- Sambridge, M. (1999). Geophysical inversion with a neighbourhood algorithm—I. Searching a parameter space. *Geophysical Journal International*, *138*(2), 479–494. <https://doi.org/10.1046/j.1365-246X.1999.00876.x>
- Samsonov, S. (2010). Topographic correction for ALOS PALSAR interferometry. *IEEE Transactions on Geoscience and Remote Sensing*, *48*(7), 3020–3027. <https://doi.org/10.1109/tgrs.2010.2043739>
- Sansosti, E., Berardino, P., Manunta, M., Serafino, F., & Fornaro, G. (2006). Geometrical SAR image registration. *IEEE Transactions on Geoscience and Remote Sensing*, *44*(10), 2861–2870. <https://doi.org/10.1109/tgrs.2006.875787>
- Segall, P. (2010). *Earthquake and volcano deformation*, pp. 432. Princeton: Princeton University Press.
- Segall, P. (2016). Reprussurization following eruption from amagma chamber with a viscoelastic aureole. *Journal of Geophysical Research: Solid Earth*, *121*, 8501–8522. <https://doi.org/10.1002/2016JB013597>
- Sepulveda, F., Dorsch, K., Lahsen, A., Bender, S., & Palacios, C. (2004). Chemical and isotopic composition of geothermal discharges from the Puyehue-Cordon Caulle area (40.5 degrees S), Southern Chile. *Geothermics*, *33*(5), 655–673. <https://doi.org/10.1016/j.geothermics.2003.10.005>
- Sepulveda, F., Lahsen, A., Bonvalot, S., Cembrano, J., Alvarado, A., & Letelier, P. (2005). Morpho-structural evolution of the Cordon Caulle geothermal region, Southern Volcanic Zone, Chile: Insights from gravity and Ar-40/Ar-39 dating. *Journal of Volcanology and Geothermal Research*, *148*(1–2), 165–189. <https://doi.org/10.1016/j.jvolgeores.2005.03.020>

- Sepulveda, F., Lahsen, A., & Powell, T. (2007). Gas geochemistry of the Cordon Caulle geothermal system, Southern Chile. *Geothermics*, 36(5), 389–420. <https://doi.org/10.1016/j.geothermics.2007.05.001>
- Siebert, L. E. E., Simkin, T. O. M., & Kimberly, P. (2010). *Volcanoes of the world* (3rd ed.): University of California Press.
- Singer, B. S., Jicha, B. R., Harper, M. A., Naranjo, J. A., Lara, L. E., & Moreno-Roa, H. (2008). Eruptive history, geochronology, and magmatic evolution of the Puyehue-Cordon Caulle volcanic complex, Chile. *Geological Society of America Bulletin*, 120(5-6), 599–618. <https://doi.org/10.1130/b26276.1>
- Singer, B. S., Le Mével, H., Licciardi, J. M., Córdova, L., Tikoff, B., Garibaldi, N., et al. (2018). Geomorphic expression of rapid holocene silicic magma reservoir growth beneath Laguna Del Maule, Chile. *Science Advances*, 4, eaat1513. <https://doi.org/10.1126/sciadv.aat1513>
- Tait, S., Jaupart, C., & Vergnolle, S. (1989). Pressure, gas content and eruption periodicity of a shallow, crystallizing magma chamber. *Earth and Planetary Science Letters*, 92(1), 107–123. [https://doi.org/10.1016/0012-821x\(89\)90025-3](https://doi.org/10.1016/0012-821x(89)90025-3)
- Tasarova, Z. A. (2007). Towards understanding the lithospheric structure of the southern Chilean subduction zone (36 degrees S–42 degrees S) and its role in the gravity field. *Geophysical Journal International*, 170(3), 995–1014. <https://doi.org/10.1111/j.1365-246X.2007.03466.x>
- Tizzani, P., Battaglia, M., Castaldo, R., Pepe, A., Zeni, G., & Lanari, R. (2015). Magma and fluid migration at Yellowstone Caldera in the last three decades inferred from inSAR, leveling, and gravity measurements. *Journal of Geophysical Research: Solid Earth*, 120, 2627–2647. <https://doi.org/10.1002/2014JB011502>
- Wendt, A., Tassara, A., Baez, J. C., Basualto, D., Lara, L. E., & García, F. (2017). Possible structural control on the 2011 eruption of Puyehue-Cordon Caulle Volcanic Complex (southern Chile) determined by inSAR, GPS and seismicity. *Geophysical Journal International*, 208(1), 134–147. <https://doi.org/10.1093/gji/ggw355>
- Wessel, P., & Smith, W. H. F. (1998). New, improved version of generic mapping tools released. *Eos Transactions American Geophysical Union*, 79(47), 579. <https://doi.org/10.1029/98EO00426>
- Williams-Jones, G., & Rymer, H. (2002). Detecting volcanic eruption precursors: A new method using gravity and deformation measurements. *Journal of Volcanology and Geothermal Research*, 113(3-4), 379–389. [https://doi.org/10.1016/s0377-0273\(01\)00272-4](https://doi.org/10.1016/s0377-0273(01)00272-4)
- Yague-Martinez, N., Prats-Iraola, P., Gonzalez, F. R., Brcic, R., Shau, R., Geudtner, D., et al. (2016). Interferometric processing of Sentinel-1 TOPS data. *IEEE Transactions on Geoscience and Remote Sensing*, 54(4), 2220–2234. <https://doi.org/10.1109/tgrs.2015.2497902>
- Yang, X. M., Davis, P. M., & Dieterich, J. H. (1988). Deformation from inflation of a dipping finite prolate spheroid in an elastic half-space as a model for volcanic stressing. *Journal of Geophysical Research*, 93(B5), 4249–4257. <https://doi.org/10.1029/JB093iB05p04249>
- Zebker, H. A., Hensley, S., Shanker, P., & Wortham, C. (2010). Geodetically accurate inSAR data processor. *IEEE Transactions on Geoscience and Remote Sensing*, 48(12), 4309–4321. <https://doi.org/10.1109/tgrs.2010.2051333>
- Zurek, J., William-Jones, G., Johnson, D., & Eggers, A. (2012). Constraining volcanic inflation at Three Sisters volcanic field in Oregon, USA, through microgravity and deformation modeling. *Geochemistry, Geophysics, Geosystems*, 13, Q10013. <https://doi.org/10.1029/2012GC004341>